Journal of Energy

VOLUME 69 Number 1 | 2020

EDITORIAL

Journal of Energy special issue: Extended papers from Second International Colloquium on Smart Grid Metrology (Smagrimet 2019), held in Split, Croatia, from 9th to 12th April 2019.

On behalf of Chairing Committee, it gives me great pleasure to present this special issue, based on selected papers presented at the Second International Colloquium on Smart Grid Metrology.

This Colloquium was organized by University of Zagreb, Faculty of electrical engineering and computing (FER) in cooperation with University of Split, Faculty of Electrical Engineering, Mechanical Engineering and Naval Architecture (FESB). It was also supported by Croatian branch of the International council for large electric power systems (HRO-CIGRE) with technical co-sponsorship from IEEE Instrumentation and Measurement Croatia Chapter.

In three Conference days more than 80 participants came from 10 countries and presented 50 papers orally in five sessions, and 20 papers in poster session. Main topics covered wide field related to smart measurements systems.

After having undergone the additional peer-review process, we believe that the papers which were selected for this special issue represent interesting research related to metrology challenges in power systems.

We would like to thank the authors for their additional efforts and the reviewers who dedicated their valuable time in selecting and reviewing these papers, both during the Conference and during the preparation of this special issue of Journal of Energy.

I wish you a pleasant time reading this Issue and hope to see you in one of next International Colloquiums on Smart Grid Metrology.

Sincerely yours,

Goran Petrović
University of Split, FESB

Martin Dadić
martin.dadic@fer.hr

Bruno Sandrić
bruno.sandric@fer.hr

Petar Mostarac
petar.mostarac@fer.hr

Roman Malarić
roman.malaric@fer.hr

University of Zagreb
Faculty of Electrical Engineering and Computing
Unska 3, 10 000 Zagreb, Croatia

A Resistive Voltage Divider for Power Measurements

SUMMARY

The paper presents a resistive voltage divider (RVD), developed for power measurements at much higher frequencies than the traditional 50 Hz. The design of the RVD and the methods of its evaluation are described. The RVD is intended to be used in a digital sampling wattmeter application based on National Instruments PXI-4461 Dynamic Signal Analyzer. The design of the divider includes individual copper guards for each resistor, driven by the auxiliary chain of resistors. To reduce the leakage currents, the PTFE terminals are applied between pins of the resistors and the printed circuit board.

KEYWORDS

resistive voltage dividers; power measurement; PXI-4461; guarding

INTRODUCTION

The resistive voltage divider (RVD) presented in this paper was designed with the main goal to be used in a digital sampling wattmeter application based on National Instruments PXI-4461 Dynamic Signal Analyzer. Since the peak input voltage of PXI 4461 Dynamic Signal Analyzer cards is constrained to 42.4 V maximum, the mains voltage (i.e. 230 V) has to be lowered using an instrument transformer or a voltage divider. In [1] a voltage instrument transformer (VIT), developed for the same application was presented. The development of the RVD was triggered with a goal to further decrease the ratio and phase angle error of the voltage transducer, thus improving the accuracy of the wattmeter.

As high-precision voltage transducers in power measurements, two types of transducers are eligible for the implementation: inductive voltage dividers (IVD) [2], and recently, resistive voltage dividers (RVD) [3-5]. The need for the much wider frequency range than traditional 50 Hz, required the use of RVDs instead of IVD. The goal was to extend the frequency bandwidth from 50 Hz to at least 3 kHz. In the audio frequency range the performance of IVDs are not satisfying, or their design is very difficult. Consequently, the frequency range of IVDs is too narrow, and the nonlinearity of their ferromagnetic core induces the harmonic distortion of the voltage [2-5]. The main purpose of this paper is to present the design of the RVD recently developed within our research group at FER-ZOEEM, with the special emphasis on the design issues as the guarding, leakage currents and the measurement procedures for the determination of the accuracy. The nominal ratio of the resistive divider is V_{in}/V_{out}=560 V/ 10 V.

The paper is organized as follows: in Section II the design principles of the RVD are described, Section III presents the measurement system based on NI 4461 cards for the characterization of the RVD. Section IV gives the measurement results of the implementation of the proposed method using a NI PXI system and Section V gives the uncertainty analysis. Finally, Section VI are conclusions.

DESIGN PRINCIPLES

Fig. 1 presents the equivalent circuit diagram of the guarded resistive divider. The parasitic capacitances are marked in dashed lines, C_0 is the input capacitance of the instrument measuring the output voltage (including cable capacitance). R_{gn} are resistances of the auxiliary chain of resistors.
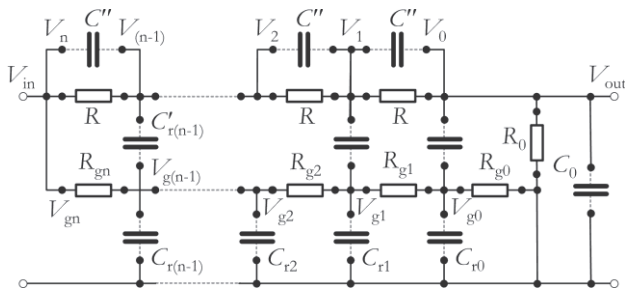

Fig. 1. Equivalent circuit diagram of the divider

The ratio of the divider is defined as:

$$V_{in} / V_{out} = nR / R_0 + 1 \qquad (1)$$

The leakage current through the main printed circuit board (PCB) could increase the phase and ratio errors of RTD. In order to reduce this effect, the resistors consisting the divider are soldered on the polytetrafluoroethylene (PTFE) insulated terminals, as depicted in the Fig. 2, similarly to the design described in [6].
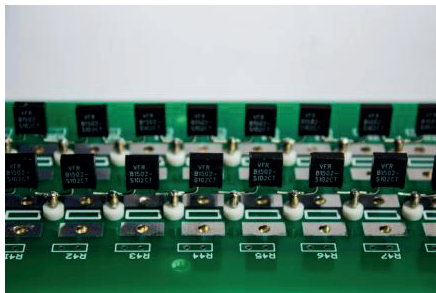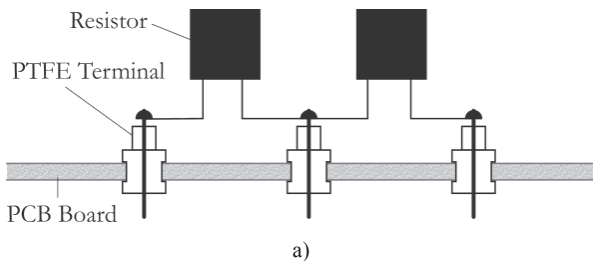
Fig. 2. Lateral view of resistor mounts: a) connection diagram b) photo of the device

The divider is consisted of $n=25$ resistors with the nominal value equal to $R=4.4$ kΩ and one resistors with the nominal value $R_0=2$ kΩ, which gives according to (1) the nominal ratio of the divider 560 V/10 V. All resistors are Vishay S series bulk metal foil (BMF), high precision resistors, model number S102C, with the ambient power rating 0.6 W at 70C. The typical temperature coefficient of resistance (TCR), declared by Vishay is ppm/C, for all resistors in the divider. The balanced TCRs in all resistors of the divider minimize the change of the ratio of the divider for different input voltages, and enables measuring of the ratio and phase angle responses of the divider at the voltage lower than nominal.

Fig. 3 presents the complete circuit diagram of the divider with the auxiliary chain of resistors and guards. Resistors $R_1 - R_{26}$ are resistors consisting the divider, with the values $R_1 - R_{25}=R$ and $R_{26}=R_0$. Resistors $R_{27} - R_{53}$ are forming the auxiliary chain. The resistors in the auxiliary chain are chosen in such a way that the guard of the each resistor in the divider is approxi-

mately at the potential equal to the potential of the half of the corresponding resistor in the main chain. In such a way the voltages at the parasitic capacitances from Fig. 1 are minimal, and consequently the influence of the parasitic capacitances are reduced. Taking into account the standard values of the resistors, the resistors in the auxiliary bridge are taken with the nominal values $R_{27}= 2.2$ kΩ, $R_{28} - R_{51}=4.7$ kΩ, $R_{52}=R_{53}=2.2$ kΩ. The resistors $R_{28} - R_{51}$ in the auxiliary chain are standard metalfilm resistors, chosen from a lot of 88 resistors. The resistances of all resistors in the set were measured prior the assembling using the 4-wire technique and a 61/2 digit multimeter Keysight 34465A, and 24 resistors with mutually closest values were chosen for the assembling. To reduce the loop area and the parasitic inductance, and in the same time to ensure the more compact physical dimensions of the divider, the resistors in the divider in the final layout of the PCB are arranged in two parallel rows (Fig. 4), connected together with a short piece of the coaxial cable Amphenol 223/U with the sleeve cable at the corresponding resistor guard potential. Fig. 4 depicts the PCB with the resistors and guards during the assembling.
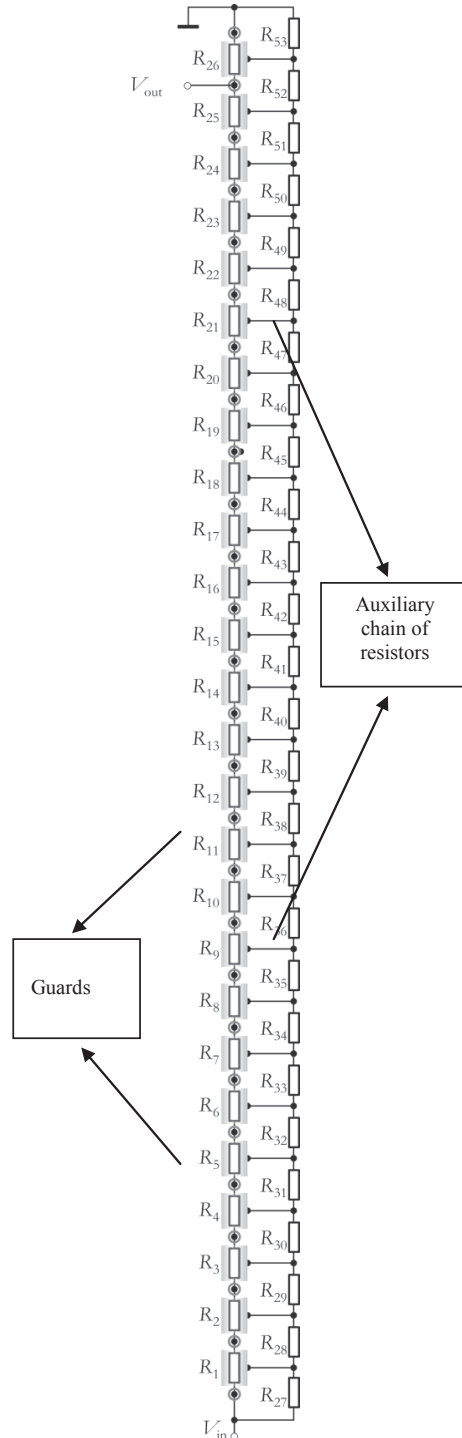

Fig. 3. Circuit diagram of the divider with the auxiliary chain of resistors and guards
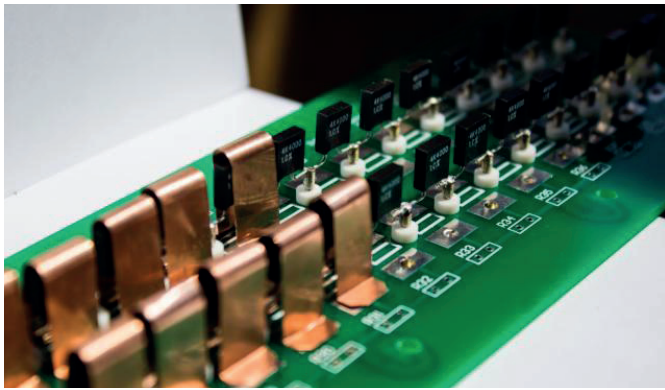
Fig. 4. The divider during assembling

MEASUREMENT SYSTEM

The measurement set-up was consisted of National Instruments PXI system, equipped with the acquisition cards (DAQ) NI PXI 4461. Time clock synchronization was accomplished using the internal PCI bus that divides 33 MHz clock. The additional synchronization of the start of the measurement process was achieved using a PXI trigger bus. Fig. 5 presents the block diagram of the measurement system, while the Fig. 6 shows the measurement set-up. The coaxial cable for the connection of the RVD to the NI 4461 card was the same that will be used in the sampling wattmeter application. In such a way, the load impedance, which affects transfer function of the divider, is the same as in the wattmeter application. The load impedance is consisted of the cable capacitance shunted by the input impedance of the card (1 MΩ paralleled by 217 pF). All inputs of the cards were configured in differential configuration.
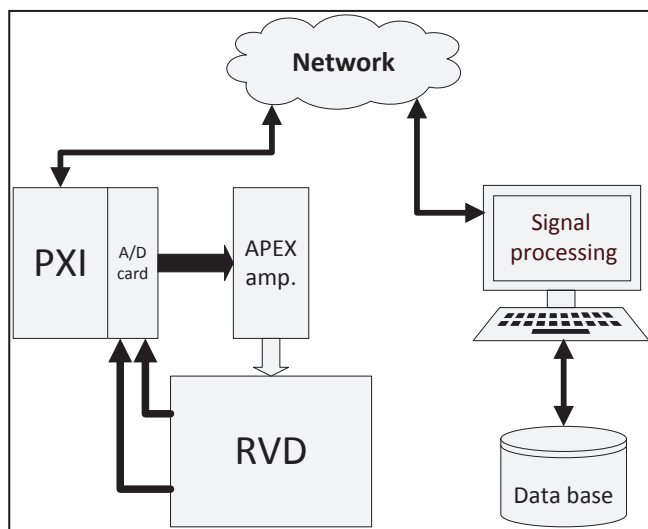
Fig. 5. Block diagram of the measurement system
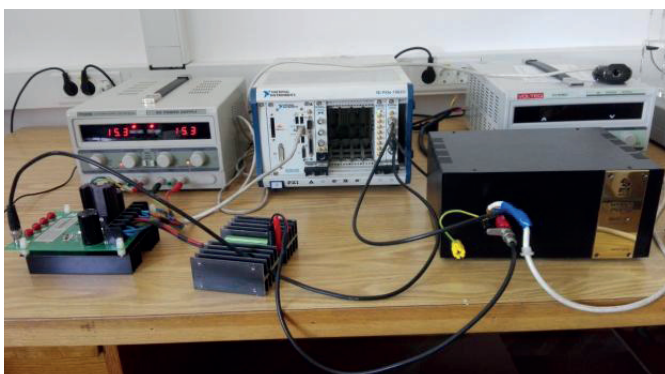
Fig. 6. Measurement set-up

The PXI system generates the stimulus signal, which is fed to the power amplifier based on Apex MP111 power operational amplifier and EK57 evaluation kit. The signal from the power amplifier is brought to the input of the divider. The input and output voltages of the RVD are brought to a NI PXI 4461 card.

The needed software was entirely programmed in-house in the NI LabView environment. The measurement process starts with the definition of the frequency range, magnitude and the set of replicate measurement for the averaging process. The communication between LabView application and the PXI system is accomplished using the Ethernet protocol and the institutional local area network (LAN), thus enabling distant start and control of the measurements. All the parameters are transferred to the PXI client that adjusts the magnitude and frequency, performs the measurements and sends the measurement results to the personal computer.

MEASUREMENT RESULTS

The measurement results are consisted of two main parts: the measurement of the ratio of the divider, and the measurement of the phase shift of the RVD.

The ratio and the phase shift are measured in a wider frequency bandwidth than defined by the international standard EN 50160, which defines measurement of the harmonics and interharmonics up to the 40th harmonic of the fundamental frequency. The frequency response of the ratio and phase shift have been measured in two ranges:

(i)   Lower range, covering two sets of first 50 harmonics of fundamental harmonics equal to 50 Hz and 60 Hz (frequencies up to 3 kHz)

(ii)   Extended range, covering the frequencies up to 50 kHz

$$k = \frac{V_{in}}{V_{out}}$$

The ratio of the divider is in all subsequent results defined as   , where V_{in} denotes the input voltage and V_{out} denotes the output voltage. The phase angle is defined as $\varphi = \alpha_{out} - \alpha_{in}$ where $\alpha_{out} -$ denotes the phase angle of the output signal and α_{in} 'denotes the phase angle of the input signal. Fig. 7 presents the ratio of the divider for the frequencies below 3 kHz. Fig. 8 presents the phase shift for the same frequency range. Fig. 9 and 10 present the ratio and the phase angle of the divider for the extended frequency range.
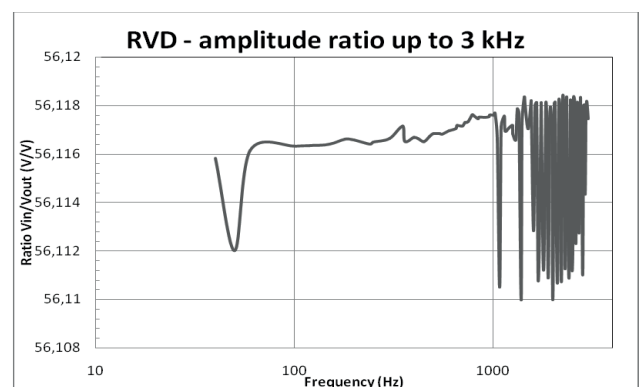
Fig. 7. Ratio of the RVD for the freqeuncies bellow 3 kHz
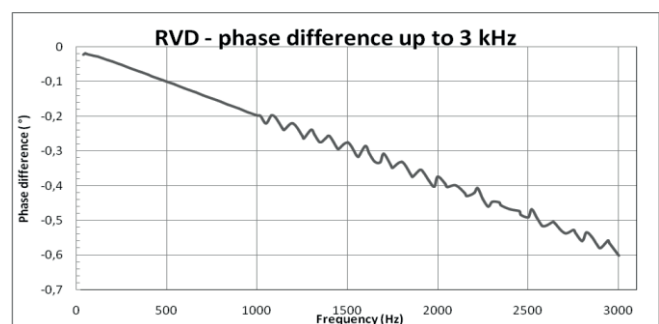
Fig. 8. Phase angle of the RVD for the freqeuncies bellow 3 kHz
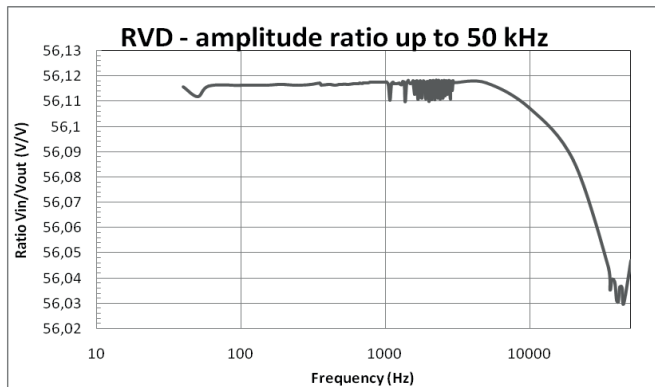
Fig. 9. Ratio of the RVD for the extended frequency range
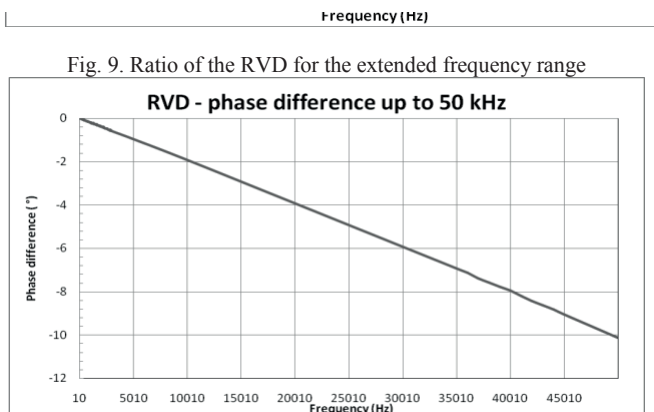
Fig. 10. Phase angle of the RVD for the extended frequency range

UNCERTAINTY ANALYSIS

The digitizer NI-PXI4461 has a two-channel 24-b sigma-delta A/D converter. A very significant parameter in characterizing a digitizer is the integral nonlinearity (INL), and its INL is smaller than 1 µV/V at frequencies higher than 40 Hz. The large INL (maximum INL is more than 80 µV/V) appears at lower frequencies, accompanied with a significant hysteresis, which can be atributed to thermal effects [7]. For 1 V signal amplitude, 1 V input range and 51.2 kS/s sampling frequency and simultaneous sampling, the digitizer's full metrological properties are as follows [8]: the temperature coefficients of the magnitude and phase are 7.4 µV/V/K and 0.000008 /K. The standard deviation of the magnitude of the voltage ratio is 2.3 µV/V. The deviation of the magnitude of the voltage ratio from the nominal value is within 3 µV/V. The phase deviation is less than 16 µ.

At 40 Hz the ratio of the RVD is 56.116 V/V where the nominal ratio is 56 V/V. The ratio of the RVD at 100 Hz is 56.116 V/V, and at 3 kHz it equals 56.117 V/V. According to Fig. 7, for the frequency range below 3 kHz it reaches the maximum value equal to 56.118 V/V and minimum value equal to 56.110 V/V, both for the frequencies between 1kHz and 3 kHz. Therefore, the maximum ratio error for the first 60 harmonics is below 0.011 %.

The phase angle at 40 Hz is -0.0211, and at 100 Hz it is -0.0250. Finally, the phase angle is -0.6010at 3 kHz. From the Fig. 6 it may be concluded that the phase angle changes linearly with the slope -0.2/kHz.

CONCLUSION

The resistive voltage divider, intended for the use in a sampling wattmeter application is developed and manufactured.

According to these results, the errors of the divider are within satisfying limits, and it yields significantly better results than a previously developed instrument voltage transformer [1] for a laboratory sampling wattmeter based on the NI 4461 DAQ. The RVD will be used in line with a set of precise current shunts of the cage type already developed at our laboratory.

The presented design is also a good basis for the further improvements that will possibly decrease the phase angle error. It can be achieved using the active elements (e.g. operational amplifiers) and compensation of the load capacitance, which is the main factor affecting the phase angle error. Those improvements will be necessary if the improved design of the RVD will be implemented in a future power standard.

REFERENCES

[1] M. Dadić, K. Petrović, R. Malarić, "FEM analysis and design of a voltage instrument transformer for digital sampling wattmeter," MIPRO 2017 Proceedings, Opatija, 2017, pp. 174-178.

[2] B.P. Kibble, G.H. Rayner, Coaxial AC Bridges, Adam Hilger, Bristol, 1984.

[3] T. Hagen and I. Budovsky, "Development of a Precision Resistive Voltage Divider for Frequencies up to 100 kHz," 2010 Conference on Precision Electromagnetic Measurements Digest (CPEM), June 13-18, 2010, Daejeon, Korea, pp. 195-196.

[4] K. E. Rydler, S. Svensson, and V. Tarasso, "Voltage Dividers with Low Phase Angle Errors for a Wideband Power Measuring System," 2012 Conference on Precision Electromagnetic Measurements Digest (CPEM), June 16-21, 2012, Ottawa, Ontario, Canada, pp. 382-383.

[5] E. Mohns, W.G. Kuerten Ihlenfeld, "A Precise Active Voltage Divider for Power Measurements," 2004 Conference on Precision Electromagnetic Measurements Digest (CPEM), June 27 – 02 July, 2004, London, UK, pp. 84-85.

[6] W. Lei, Zhu Zongwen, H. Hongtao, L. Min, L. Lijuan, L. Zuliang, "Resistive Voltage Divider with Two Stage Voltage Buffer for Harmonic Measurement," 2012 Conference on Precision Electromagnetic Measurements Digest (CPEM), 01–06 July, 2012, Washington DC, USA, pp. 148-149.

[7] F. Overney, A. Ruefenacht, J.P. Braun, B. Jeanneret and P.S Wright, "Characterization of Metrological Grade Analog-to-Digital Converters Using a Programmable Josephson Voltage Standard," IEEE Trans. Instrum. Meas., vol. 60, no. 7, pp. 2172-2177, July 2011.

[8] R. Rybski, J. Kaczmarek, M. Koziol, "A High-Resolution PXI Digitizer for a Low-Value_Resistor Calibration System, " IEEE

[9] Trans. Instrum. Meas., vol. 62, no. 6, pp. 1783-1788, June 2013.

[10] M. Dadić, P. Mostarac, R. Malarić, "Wiener Filtering for Real-Time DSP Compensation of Current Transformers over a Wide Frequency Range," IEEE Transactions on Instrumentation and Measurement, vol. 66, no. 11, pp. 3023-3031, November 2017.

Antonijo Kunac

Marin Despalatović

Dario Šantić

Department of Electrical Engineering
FESB
University of Split
Croatia

Synchrophasors Determination Based on Interpolated FFT Algorithm

SUMMARY

Within the standard IEEE C37.118 applications and proposed hardware structure of a phasor measurement unit (PMU) are described. This paper presents the concept of the system for measuring and transferring synchrophasors from a theoretical aspect. Synchrophasor algorithms are developed in MATLAB/Simulink for the purpose of easier verification and hardware deployment on today's market available and affordable real time development kits. Analysis of the synchrophasor measurement process is performed gradually. Firstly, by defining the synchrophasor based on three-phase to $\alpha\beta$-transformation and then introducing a discrete Fourier transform (DFT) based on synchrophasor estimation algorithm. Later, accompanying adverse effects resulting from its application are analyzed by means of simulation. To increase accuracy and improve estimation algorithm interpolated discrete Fourier transform (IpDFT) with and without windowing technique is used. To further optimize algorithm performance convolution sum in recursive form has been implemented instead of classical DFT approach. This study was carried out in order to validate described measurement system for the monitoring of transients during island operation of a local power electric system. Finally, simulation and experimental results including error analysis are also presented.

KEYWORDS

Digital signal processing, Discrete Fourier transforms, Modeling, Phasor measurement unit, Simulation

INTRODUCTION

The development of information and communication technology has provided preconditions for automatization of the electric power system. Moreover, significant progress in managing and controlling the operation of the complete system as well as improving the quality and reliability of the electricity supply have also been achieved.

The classic approach used to manage and monitor electric power system is the supervisory control and data acquisition (SCADA) system. It is a system whose upgrades has reached their limits and are not so ''open'' to the latest technology. Therefore, intensive work on developing new remote management systems based on smart grid solutions is still ongoing process. Remote control and monitoring systems play a major role in determining optimal solutions for failures in electrical power systems, which significantly reduces investment and maintenance costs, as well as reducing losses due to interruptions and undelivered electricity. The quality of electricity is determined by the following parameters: voltage quality, supply reliability and service quality. Because of the increasingly stringent requirements for electricity quality, intelligent electronic device (IED) development is indispensable. Some of IEDs used for this purpose are: remote terminal unit (RTU), digital multimeters, power quality (PQ) monitors, etc.

Currently, the latest and most promising version of the IED is a phasor measurement unit (PMU). PMU represent a technology that has enabled insight into the real-time (RT) electrical power system dynamics [1], [2]. In this paper PMU algorithms for synchrophasor estimation are developed in MATLAB/Simulink.

The main task of the algorithm is to estimate parameters of the fundamental tone of the signal (amplitude, frequency and phase) [3]. Discrete Fourier transform (DFT) is the most commonly used method for identifying the fundamental tone of the signal [4], [5]. Generally, the advantages of the DFT approach are low computational complexity and harmonic rejection, while the drawbacks are spectral leakage and aliasing. In this paper to counteract these effects Fourier analysis and interpolated discrete Fourier transform (IpDFT) have been used [6]. This algorithm combined with and without use of windowing technique as well as use of convolution sum in recursive form will be described in the following sections.

7

Antonijo Kunac, Marin Despalatović, Dario Šantić, Synchrophasors Determination Based on Interpolated FFT Algorithm, Journal of Energy, vol. 69 Number 1 (2020), p. 7–12

DIGITAL SIGNAL PROCESSING

DFT algorithms

Main steps when applying a DFT-based digital signal processing technique to a continuous signal $x(t)$ are shown in Fig. 1.
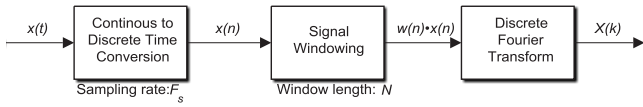
Block diagram of digital signal processing [3].

The Fourier transform (FT) of a continuous time-function $x(t)$ is defined as follows

$$X(f) = \int_{-\infty}^{\infty} x(t) \cdot e^{-j2\pi ft}\, dt \tag{1}$$

As can be seen, FT is used to transform a continuous time-domain function $x(t)$ to a continuous frequency-domain function $X(f)$. In order to implement signal processing algorithms into a digital system, conversion of an analog signal to its digital representation must be performed [3].

Therefore, the discrete-time FT (DTFT) allows a transformation of a discrete sequence of infinite length $x(n)$ into a continuous frequency-domain function

$$X(f) = \sum_{n=-\infty}^{\infty} x(n) \cdot e^{-j2\pi fn} \tag{2}$$

Since upper expression is continuous and infinite it is not appropriate for digital signal processing and cannot be applied for real-time applications. The discrete Fourier series (DFS) is another way to transform an infinite continuous periodic sequence in the frequency domain. When the DFS is used to transform a generic discrete periodic finite-length sequence of samples, it is called the DFT [8].

Scalar to vector representation of three-phase system

For the sake of simplification, we assume balanced three-phase system of instantaneous voltages

$$v_a = A(t) \cdot \cos(\phi(t)) \tag{3}$$
$$v_b = A(t) \cdot \cos(\phi(t) - 2\pi/3)$$
$$v_c = A(t) \cdot \cos(\phi(t) + 2\pi/3)$$

where $A(t)$ is the arbitrary magnitude function of time, while phase angle function may be expressed as

$$\phi(t) = 2\pi \int_0^t f(t)dt + \phi(0) \tag{4}$$

where (0) is the initial phase angle value, and $f(t)$ is the arbitrary frequency function of time. For the purpose of following analysis, we assume

$$f(t) = f_o + \Delta F \cdot \cos \Omega t \tag{5}$$

where fo is the average grid frequency assumed to be equal to 50 Hz, ΔF is the peak value of frequency deviation, and Ω is the angular modulation frequency of the fundamental harmonic fo, respectively. If (5) is inserted in (4), assuming zero phase initial value and after simplification, we obtain

$$\phi(t) = 2\pi f_o t + \frac{\Delta F}{\Omega} \cdot \sin \Omega t \tag{6}$$

Since balanced three-phase system is assumed, it is convenient to apply $\alpha\beta$-transformation on abc variables, which is equal to reduction of three to two-phase system [9]. Also known as the Clarke transformation, after applying it to scalar representation (3) the following complex voltage time function, i.e. synchrophasor, may be written

$$v(t) = v_\alpha(t) + j v_\beta(t) \tag{7}$$

where the real and imaginary parts on the right-hand side of equation correspond to the transformed α and β voltage components, respecti-

vely. Instead of using rectangular coordinate system in (7) for the ease of analysis more appropriate is polar coordinate system that gives

$$v(t) = A(t) \cdot e^{-j\phi(t)} \tag{8}$$

Thus, one should observe that for the three-phase system $\alpha\beta$-transformation is equal to the Hilbert's transform for single phase system. In other words, any real signal can be transformed using Hilbert's transform into a so-called analytical signal [8]. Additionally, (8) is equivalent to the reference signal used for space vector modulation control of three-phase inverters [9], [10].

Discretization of continuous time signals

A discrete-time signal of (8), produced by a sampling process characterized with the sampling period Ts, is

$$v[n] = A[n] \cdot \exp\left(j2\pi\left(f_o nT_s + (\Delta F/\Omega) \cdot \sin(\Omega nT_s)\right)\right) \tag{9}$$

where $0 \le n \le N$-1 is the sample number, and N is the total number of observed samples. Hence, the input signal is sliced in blocks containing N samples.

DFT of the observed signal is calculated in discrete points $k = 0, ..., N$-1 according to the following expression

$$V[k] = \sum_{n=0}^{N-1} v[n] \cdot e^{-j\frac{2\pi k}{N}n} \tag{10}$$

For the case of pure sinusoidal three-phase system with fundamental period that is an integer multiple of the sample period ($To = NTs$) only the fundamental harmonic appears in the frequency spectrum as is shown in Fig. 2. When the harmonic fundamental period is not equal to the length of observed signal block sequence spectral leakage occurs even in a case when only a one tone is given as is illustrated in Fig. 3.
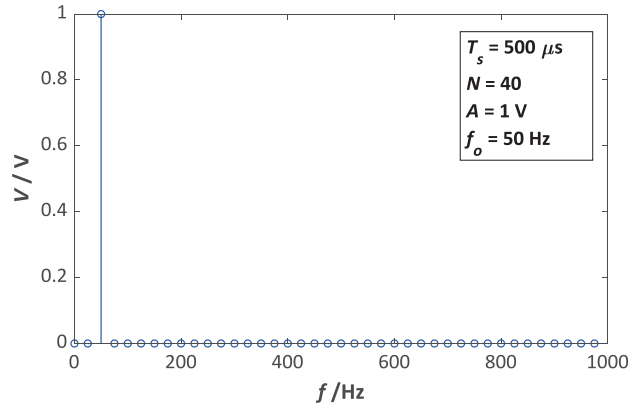

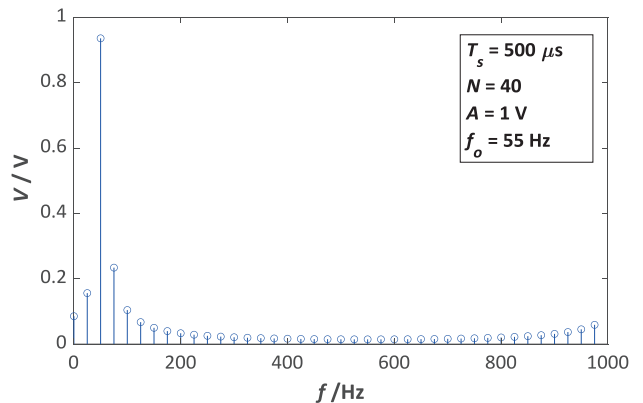Fig 2. Signal spectrum without spectral leakage.

Fig 3. Signal spectrum with spectral leakage.

Interpolation algorithm

If the length of window does not contain an integer number of samples, i.e. it is not equal to the voltage fundamental period, leakage occurs. Because of that, the main tone of the signal is located between two consecutive DFT bins. For a such case, interpolation algorithms are used to obtain accurate magnitude and frequency value of the voltage fundamental harmonic. In literature one can find a variety of interpolation formulas that can be used to derive the actual signal frequency from such a spectrum. The only requirement is that there is only a one frequency component in the observed band.

The simplest interpolation technique is to fit the parabola through three points and search for its maximum. The parabola equation used to estimate voltage magnitude is defined as follows

$$|V(\lambda)| = c\lambda^2 + b\lambda + a \tag{11}$$

where λ is the intermediate variable in auxiliary coordinate system used to determine the exact frequency of the fundamental harmonic. To determine parabolic coefficients (a, b, c), system of three equations with three unknowns must be solved

$$\begin{bmatrix} 1 & \lambda & \lambda^2 \\ 1 & \lambda & \lambda^2 \\ 1 & \lambda & \lambda^2 \end{bmatrix} \begin{bmatrix} a \\ b \\ c \end{bmatrix} = \begin{bmatrix} |V[k_m-1]| \\ |V[k_m]| \\ |V[k_m+1]| \end{bmatrix} \tag{12}$$

where km is the sample index of the DFT's spectrum characterized by the magnitude $|V[km]|$ of the middle frequency bin as is designated in Fig. 4. $|V[km-1]|$ is the neighboring tone on the left side, while $|V[km+1]|$ is the neighboring tone on the right side.

Square matrix on the left side of (12) takes the simplest form if the auxiliary ordinate ($\lambda = 0$) passes through the middle frequency bin (km) and becomes

$$J = \begin{bmatrix} 1 & -1 & 1 \\ 1 & 0 & 0 \\ 1 & 1 & 1 \end{bmatrix} \tag{13}$$

To obtain solution of (12) one should calculate the inverse matrix of (13)

$$J^{-1} = \begin{bmatrix} 0 & 1 & 0 \\ -0.5 & 0 & 0.5 \\ 0.5 & -1 & 0.5 \end{bmatrix} \tag{14}$$

after which determination of parabola coefficients is straight forward

$$a = |V[k_m]| \tag{15}$$
$$b = 0.5 \cdot |V[k_m+1]| - 0.5 \cdot |V[k_m-1]|$$
$$c = 0.5 \cdot |V[k_m-1]| + 0.5 \cdot |V[k_m+1]| - |V[k_m]|$$

The maximum of the parabola (11) can be founded when its first derivative equals zero

$$2c\lambda_m + b = 0 \tag{16}$$

where fractional term

$$\lambda_m = \frac{|V[k_m-1]| - |V[k_m+1]|}{2 \cdot (|V[k_m-1]| - 2|V[k_m]| + |V[k_m+1]|)} \tag{17}$$

must satisfy $|\lambda m| < 1$. Once fractional term is known the maximum of the parabola is found for sample

$$k_{peak} = k_m + \lambda_m \tag{18}$$
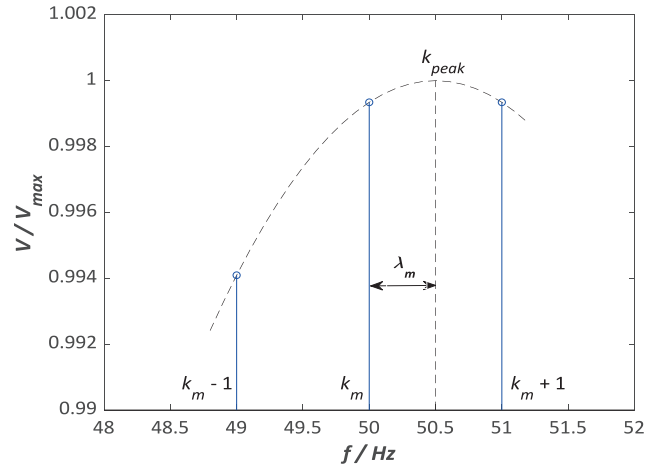
as is illustrated in Fig. 4.

Fig 4. Illustration of parabola interpolation algorithm.

If we assume that duration of observed signal block sequence is equal to 40 ms, the DFT frequency resolution equals 25 Hz. This results with 25, 50 and 75 Hz bins on the frequency axis. Since interesting component of grid voltage is usually in vicinity of 50 Hz there is no need to count FFT at all points except in, for instance, 49, 50 and 51 Hz bins as is shown in Fig. 4. Instead of using a one second duration of signal block sequence to obtain frequency resolution of 1 Hz one can use the following convolution expression

$$V_M = \sum_{n=0}^{N-1} v[n] \cdot e^{-j\frac{2\pi M}{N}n} \tag{19}$$

to obtain corresponding frequency bins where $M = \{49, 50, 51\}$. The main advantage of (19) in comparison to DFT calculation is a shorter signal processing time since only three bins need to be processed and the length of block sequence needs to be at least 20 ms.

Windowing technique

To avoid consequences of spectral leakage and to improve accuracy of voltage magnitude and frequency estimated values a windowing technique is utilized [3], [7], [8]. Instead of (10), DFT spectrum of observed data block may be computed using a preselected windowing function as follows

$$V[k] = \frac{1}{B} \sum_{n=0}^{N-1} v[n] \cdot w[n] \cdot e^{-j\frac{2\pi k}{N}n} \tag{20}$$

where $w[n]$ is usually the discrete Hanning windowing function that is used to extract a portion of the infinite length original sequence, and B is the DFT's normalization factor

$$B = \sum_{n=0}^{N-1} w[n] \tag{21}$$

It is important to note that fractional correction term λm is more accurate when windowing technique is applied. However, authors' focus is on how to find the correction term for determining the "accurate" frequency of the fundamental spectrum tone using computationally the most effective algorithm, which rectangular window is in comparison to Hanning window. This approach gives satisfactory accuracy and responsiveness as will be shown later in the paper.

DESCRIPTION OF MODEL

Performance analysis of estimation algorithms has been carried out in MATLAB/Simulink environment by xPC Target model shown in Fig. 7 [11]. Presented model enables user to perform pure simulations on local (Host) computer as well as to perform rapid prototyping, i.e. hardware-in-the-loop testing on remote (Target) computer equipped with I/O hardware units. The mode of operation depends entirely on position of the two manual switches shown in Fig. 7.

The model consists of three parts. The first part (middle of Fig. 7.) comprises of setpoint magnitude and frequency generator in accordance with

(4)-(9). The main task of this part is to generate cosine and sine reference signals with arbitrary magnitude and frequency that acts as a rough approximation of the actual situation in the real power grid. At the same time these signals are also connected with analog output (D/A) block so they can be monitored as process variables by independent third-party measurement equipment. When manual switch is in "Simulation only" position these signals serve as inputs to estimation algorithm. Since reference signals are a priori known this mode of operation serves for theoretical accuracy and responsivity evaluation.

The second part (top of Fig. 7.) encompasses hardware analog input (A/D) block with offset and gain blocks for tuning accuracy in combination with blocks for transformation of two line-to-line voltages (Uac, Ubc) into $\alpha\beta$ variables, i.e. complex signal [9]. Manual switch position "Calibration" determines independent calibration procedure while position "Measurement" determines direct grid voltage syncrophasor measurements.

Finally, the third part (bottom of Fig. 7.) encompasses estimation algorithm. After generating a complex signal that represents transformed $\alpha\beta$ variables of three-phase voltage system, independently of switch position "Simulation only" or "Calibration/Measurement", three convolution sums for 49, 50 and 51 Hz are calculated. As can be seen for optimal deployment regarding computation and memory requirements it is preferable to implement convolution sum (19) in recursive form as is shown in Fig. 5.
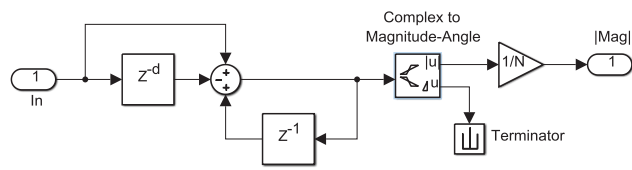
Fig. 5 Recursive model of convolution sum (19), delay d = N.

SIMULATION RESULTS

Validity of previously described model as well as interpolation algorithms has been confirmed by numerous simulations under various grid operating conditions. Representative response on how estimated frequency tracks setpoint frequency is shown in Fig. 6.

To quantify quality of frequency estimation error the following expression is used

$$\Delta f = \left(f_{est} / f_{set} - 1 \right) \times 100 \, \% \tag{25}$$

where f_{est} is the estimated frequency value, and f_{set} is the frequency setpoint.
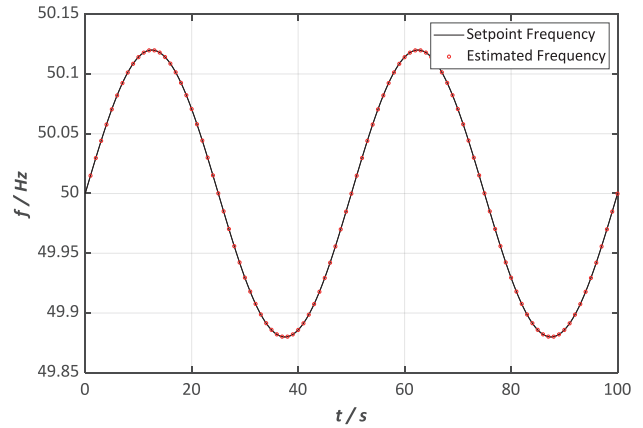
Fig. 6 Comparison of setpoint and estimated frequency for ΔF = 0.12 Hz and (Ω/2π) = 20 mHz

To demonstrate interpolation algorithm (17) and (18) effectiveness, the maximum absolute value of estimation error versus angular modulation frequency in (5) is observed. Obviously, estimation error rises as modulation frequency rises, and according to Fig. 8 this dependency is linear. As can be seen for modulation frequency of 2 Hz expected estimation error is less than 0.03 %. One should bear in mind that maximum value of grid voltage modulation frequency most of the time is less than 20 mHz, i.e. two orders of magnitude lower value. Thus, it may be concluded that presented estimation procedure is very accurate. The same is also valid for the interpolation algorithm based on windowing technique but computation time is longer while expected estimation error is less than the one shown in Fig. 8, i.e. the slope of line is lower.
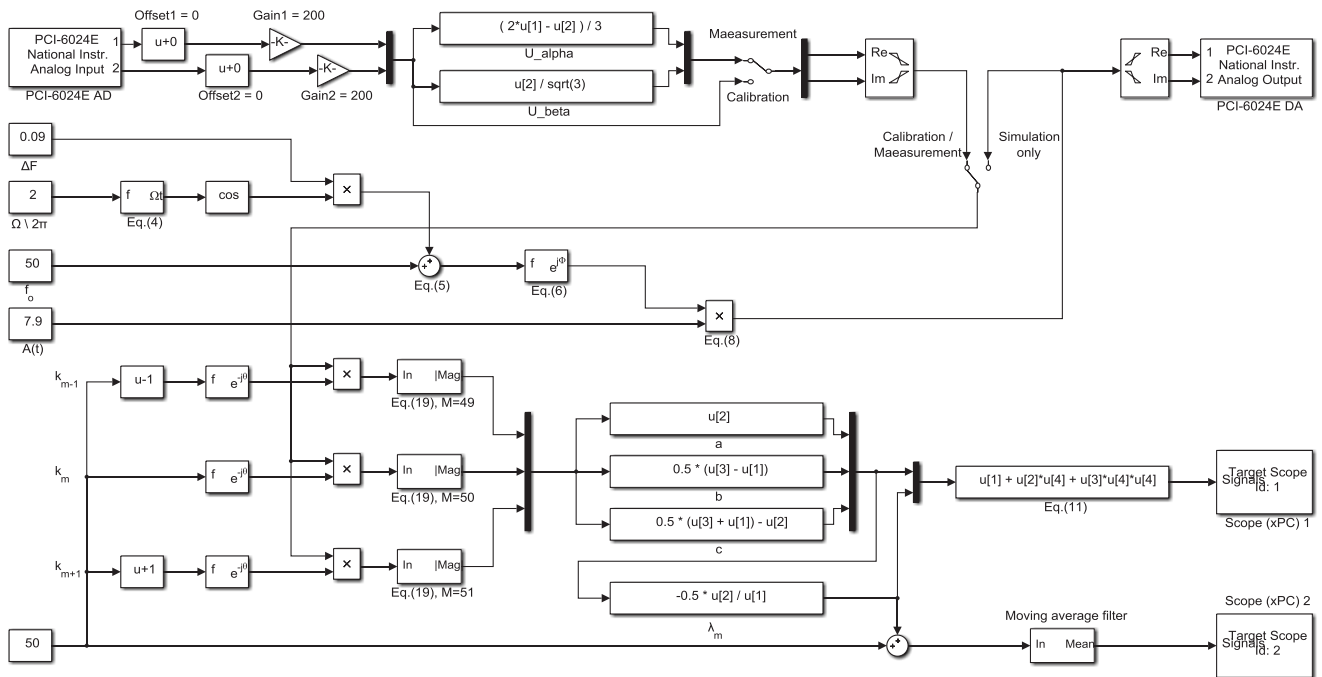
Fig. 7 xPC Target simulation model for determination of synchrophasors in MATLAB/Simulink.
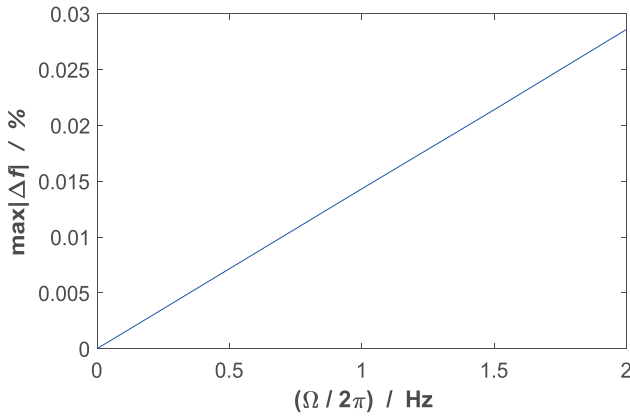
Fig. 8 Maximum estimation error versus modulation frequency.

FDig. 10 Waveforms of test signals during testbed calibration procedure.

EXPERIMENTAL SETUP

The main part of the experimental setup is xPC Target platform in MA-TLAB/Simulink environment which enables rapid hardware-in-the-loop prototyping at affordable price-to-performance ratio. Laboratory testbed for grid voltage synchrophasor measurement is shown in Fig. 9. The standalone xPC Target computer showing real-time voltage monitoring is shown on the left side of the photography while on the right side is the Host PC showing xPC Target model on the middle screen and oscilloscope software on the right screen. For interaction with outside world 12-bit National Instruments' I/O data acquisition board PCI-6024E, located within desktop Target PC, is used. Since analog inputs' voltage measurement range are ±10 V a two 25 MHz bandwidth Pico Technology's TA057 differential probes were used for grid voltage measurement. For voltage and frequency calibration purposes independent measuring equipment consisting of Hewlett Packard's 3457A digital multimeter in combination with TiePie's HandyScope HS5 digital USB oscilloscope were used.
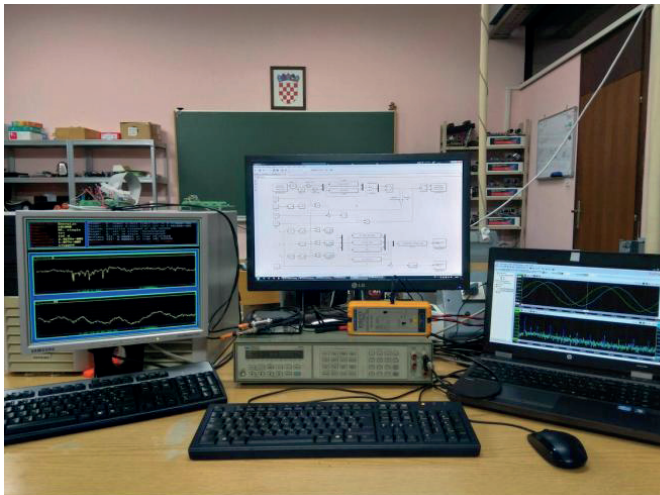

Fig. 9 Laboratory setup for grid voltage synchrophasor monitoring.

EXPERIMENTAL RESULTS

Prior to recording grid voltage measurements calibration of laboratory setup was performed. As a first stage, internal calibration procedure was carried out in order to verify estimation algorithm accuracy and compensate for D/A and A/D offsets and gains. This is done simply by putting the left manual switch to "Calibration" position and the right switch in Fig. 7 to "Calibration/Measurement" position, and directly connecting analog outputs with corresponding analog inputs. At the same time multimeter and oscilloscope are also connected in parallel with board's I/O. Steady-state voltage waveforms of test signals during testbed calibration procedure are shown in Fig. 10. Response to dynamic frequency setpoint change obtained from standalone xPC Target system is shown in Fig. 11 which validates effectiveness of proposed estimation algorithm.
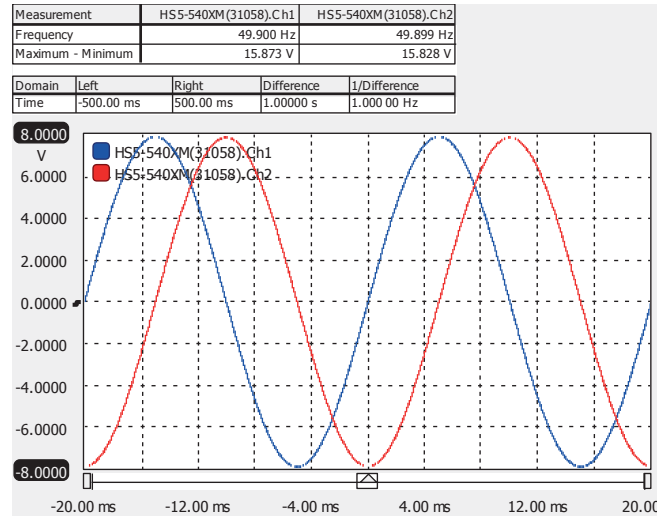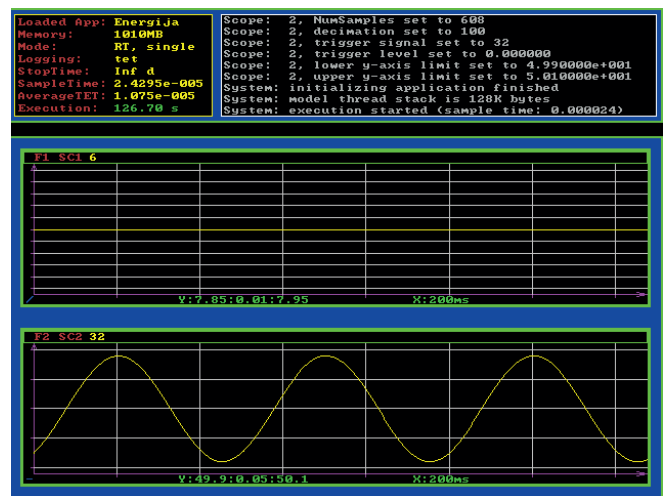
Fig. 11 Online monitoring of synchrophasor during calibration procedure for ΔF = 0.09 Hz and (Ω/2π) = 2 Hz.

In the second stage, after physically disconnecting analog inputs and outputs, external calibration procedure was carried out using programmable function generator under known conditions. For this purpose, the same USB oscilloscope is used since it is equipped with arbitrary waveform generator. Again, these measurements served as additional confirmation of calibration procedure.

After tuning offsets and gains steady-state voltage accuracy of 0.1 % of full-scale range and 1 mHz frequency accuracy were achieved. It should be emphasized that during transients estimated frequency value lags setpoint value by 10 ms, i.e. $N/2$ samples.

In order to encompass grid voltage measurement range separately calibrated differential probes with gains equal to 200 are connected to corresponding analog inputs. Steady- state waveforms of the line-to-line grid voltages during laboratory experiments are shown in Fig. 12. One can see that actual measured voltages can be unbalanced, and their frequency spectrums have higher harmonics besides the fundamental one. It should be pointed out that shown line-to-line voltages are deliberately chosen in a such a way to apply following $\alpha\beta$ transformation formulas [9]

$$(22)$$

$$u_\alpha = \frac{2}{3}u_{ac} - \frac{1}{3}u_{bc}$$

$$u_\beta = \frac{\sqrt{3}}{3}u_{bc}$$

while the zero-sequence voltage is always equal to zero.

Measurement	HS5-540XM(31058).Uac	HS5-540XM(31058).Ubc
RMS	415.28 V	414.55 V
Frequency	50.010 Hz	50.010 Hz

Domain	Left	Right	Difference	1/Difference
Time	-500.00 ms	500.00 ms	1.0000 s	1.000 00 Hz

Fig. 12 Grid voltage waveforms during laboratory experiments.

Fig. 13 shows online monitoring of the grid voltage synchrophasor in FESB laboratory during 240 s interval. Due to presence of the grid voltage higher harmonics as well as to magnitude asymmetry, estimated frequency value besides steady-state dc value also has periodic ac value. A low pass moving average filter is used to eliminate the latter component (Fig. 7). This filter introduces additional lag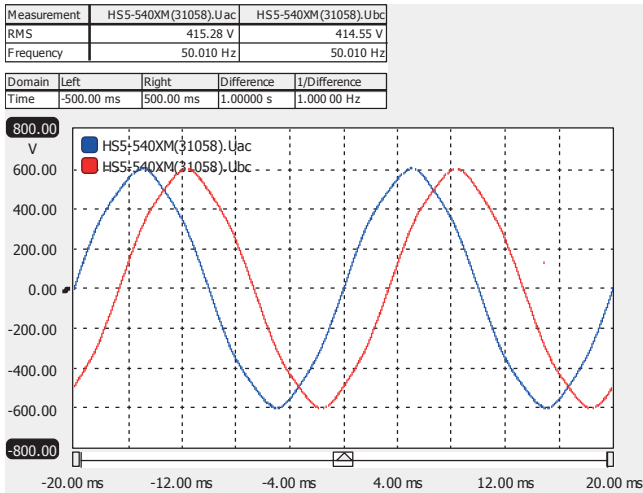ging into estimation process equal to 10 ms, which aggregates in total to the period of the fundamental harmonic, i.e. to N samples.
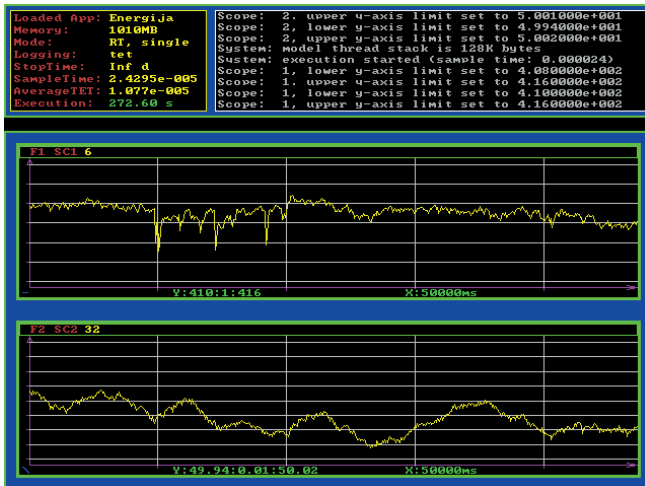

Fig. 13 Grid voltage synchrophasor online monitoring in FESB laboratory.

Note that the grid voltage magnitude ac component is significantly lower in comparison to the steady-state value. Thus, for the sake of simplicity the magnitude low-pass filter is omitted in Fig. 7.

Finally, representative response in Fig. 13 is selected as it shows a part of 7-minute interval where average grid frequency was approximately 49.97 Hz, i.e. it deviates 30 mHz from the rated value. Future work will involve inclusion of additional voltage statistics into the real-time monitoring system to ease analysis.

CONCLUSION

This paper presents a procedure for monitoring syncrophasor of the fundamental voltage harmonic based on the IpDFT algorithm. Simulation analysis performed in MATLAB/Simulink demonstrate accuracy and responsivity of the algorithm given in the paper. In addition, calibration procedure performed using programmable function generator under known conditions as well as experimental analysis of grid voltage has also been carried out. The main advantage of implemented convolution sum technique realized in recursive form in comparison to classic DFT algorithms is speed and memory optimization. This study has been carried out in order to validate described measurement system for the monitoring of transients during island operation of a "small" local power electric system. Deployment of the presented algorithm to FPGA as well as introduction of a new functionalities as part of developing PQ monitoring system for field tests will be included in future work.

ACKNOWLEDGMENT

REFERENCES

[1] Q. Guo, and R. Gan, "An Arbitary-Resampling-based synchrophasor measurement algorithm in compliance with IEEE Std C37.118.1a-2014: Design, implementation, and validation", IEEE/PES Transmission and Distribution Conference and Exposition (T&D), July 2016.

[2] "IEEE Standard for Synchrophasor Measurments for Power Systems", IEEE Std C37.118.2-2011 (Revison of IEEE Std C37.118-2005), Dec. 2011.

[3] P. Romano, "DFT-based Synchrophasor Estimation Algorithms and their Integration in Advanced Phasor Measurement Units for the Real-time Monitoring of Active Distribution Networks ", PhD thesis, EPFL, Lausanne, 2016.

[4] P. Romano, and M. Paolone, "Enchanced Interpolated-DFT for Synchrophasor Estimation in FPGAs: Theory, Implementation, and Validation of a PMU Prototype", IEEE Transaction on Instrumentation and Measurement, vol. 63, pp. 2824-2836, Dec. 2014.

[5] P. Romano, M. Paolone, J. Arnold, and R. Piacentini, "An Interpolated-DFT Synchrophasor Estimation Algorithm and Its Implementation in an FPGA-based PMU Prototype", IEEE Power & Energy Society General Meeting, Nov. 2013.

[6] A.G. Phadke, and J.S.Thorp, "Synchronized Phasor Measurements and Their Applications", Springer Science+Business Media, LLC, 2008.

[7] G. Andria, M. Savino and A. Trotta: "Windows and interpolation algorithms to improve electrical measurement accuracy", IEEE Transactions on Instrumentation and Measurement, vol.38, pp. 856-863, 1989.

[8] M. Mandal, and A. Asif.: "Continuous and Discrete Time Signals and Systems", Cambridge University Press, New York, NY, 2007.

[9] A. M. Trzynadlowski: "Control of Induction Motors", Academic Press, San Diego, CA, 2001.

[10] D. G. Holmes, and T. A. Lipo: "Pulse Width Modulation for Power Converters", IEEE Press, Piscataway, NJ, 2003.

[11] "xPC Target User's Guide", The MathWorks Inc, Natick, MA, 2013.

Ivan Višić
Pro Integris, Split, Croatia, ivan.visic@prointegris.hr

Ivan Strnad
Pro Integris, Zagreb, Croatia, ivan.strnad@prointegris.hr

Tihomir Tonković
Veski, Zagreb, Croatia, tihomir.tonkovic@veski.hr

Real Time Load Angle Application for Synchronous Generator Protection Purposes

SUMMARY

The out-of-step protection function is one of the key functions in generator protection. This function detects the loss of generator synchronism, and when such a fault occurs, it is necessary to disconnect the generator from the rest of the system as soon as possible in order to avoid major damages. The algorithms used in the out-of-step protection functions are based on the measurements of generator impedances and they use the impedance vectors to check if all stability criterions are met. This paper describes a new approach to realizing the out-of-step generator protection function by using the direct load angle measurement. The idea behind applying the real time load angle measurement is to faster detect the loss of synchronism.

KEYWORDS

electrical load angle, synchronous generator, air gap, out of step generator protection.

INTRODUCTION

The generator protection device is one of the key components of every power plant. Its goal is to use input parameters (measurements and signals) and built-in algorithms to protect the generator from faults in auxiliary generator systems, faults in the grid and internal generator faults. Different functions or algorithms are used in the generator protection device to protect the generator from different types of faults. These algorithms are implemented in numeric protection relays that, in addition to carrying out the algorithms, gather and process input data and (depending on the algorithm results) act towards other systems to prevent generator damage. One of the functions with a major role in generator protection is the out-of-step protection function, which is currently implemented by assessing the generator stability based on the monotony, continuity and uniformity of impedance change [1],[2]. In certain operational situations (important power line outages, short circuits) in power systems, disturbances which can cause the loss of synchronism within the power system or between mutually connected systems can occur. If such a loss of synchronism is manifested, the asynchronous areas have to be isolated before the generator is damaged and other outages start occurring throughout the system. When the loss of generator synchronism occurs, high amplitude currents cause strains in generator windings as well as mechanical strains that can lead to generator and turbine damages [5]. Generator faults caused by such malfunctions usually bring significant financial costs manifested by expensive repairs and revenue loss due to production interruptions. The-

refore, it is important to identify the fault and shut the turbine and generator as soon as possible [3].

Considering the fact that the generator load angle is a value that specifically indicates the position of the generator operating point in relation to the border of stable operation, the possibility of using the load angle for generator protection purposes opens up [6]. In addition, load angle can be used in the following applications:

- maintenance of stability of power system through the action on generator excitation system,

- determination of real time generator capability chart,

- torsional dynamics of generator (analysis during power swing or electrical transient load),

- electro-mechanical resonance detection,

- measurement of losses (stator core and mechanical).

Although the load angle is a very reliable indicator of system stability, it is still insufficiently used in generator protection, and one of the reasons for this situation is the complexity of its direct measurement [4].

Taking into account the above mentioned, the paper describes the method used for real time measurements of the load angle of synchronous generator. The paper defines a new approach to using the load angle for
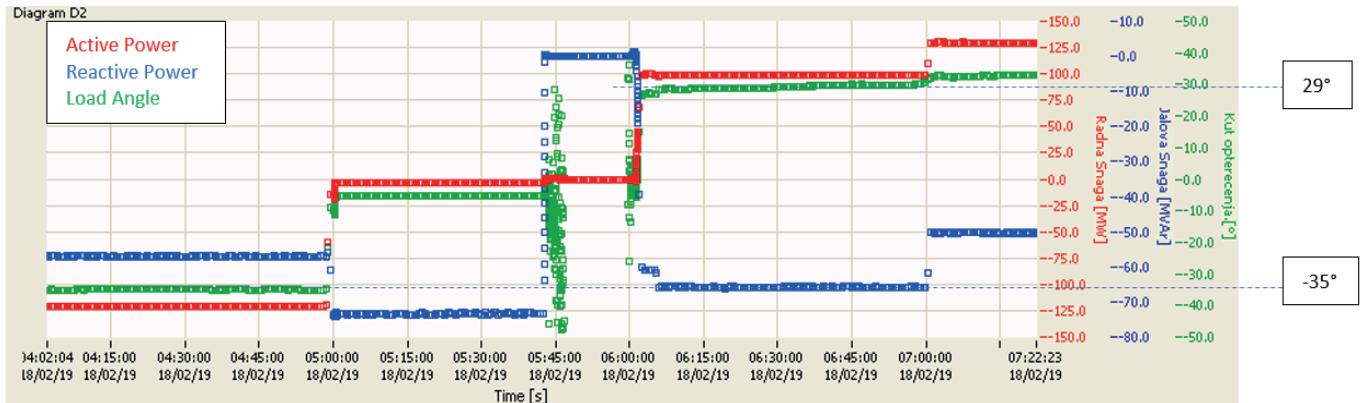
Fig. 1. Graphical representation that shows relation of rotor position, magnetic field and load angle

the generator out-of-step protection function. Additionally, the paper overviews the existing algorithms for synchronous generators' out-of-step protection function used in today's generator protection relays.

LOAD ANGLE MEASUREMENT

The electrical load angle (δ) is the angle between induced EMF and terminal voltage or the angle between rotor and stator magnetic fields. The magnetic field of a synchronous generator rotates at synchronous speed and induces a rotating magnetic field in a stator. These two fields are not completely aligned. The stator field lags behind the rotor field. This lagging is expressed in the load angle.

Fig. 1. shows the relation of rotor position, magnetic field and load angle. The generated power is directly proportional to the sine value of this angle.

The load angle is also a direct representative of magnetic field torsional stiffness inside the air gap as well as of generator stability in operation (e.g. out-of-step). On-line measurement of the load angle (static and dynamic) is of great importance when determining actual working parameters of a generator when combined with the on-line capability chart (P-Q chart). Load angle, if measured with fine resolution, can be used to determine losses of a generator. It is also a key parameter in understanding torsional dynamics of a generator where magnetic field stiffness influences dynamic response of the generator.

The load angle can be measured by either using the shaft encoder or air gap sensor placed inside the stator and the signal of terminal voltage on one phase (it doesn't matter which.). In our research, we use the air gap sensor method for measuring the load angle. The air gap sensor gives more stable and precise information on the rotor position compared to the

shaft encoder due to the small radius of the shaft encoder ring compared to the rotor radius. Consequently, the load angle calculation is more precise [7]- [10].

The air gap sensor measures the distance between the stator and rotor poles. It produces a signal whose frequency is twice the grid frequency and is a good representation of rotor position. Since the rotor position is in phase with induced EMF, it can be used to determine the value of the load angle together with a signal of terminal voltage.

Fig. 2. shows the measurement results and the relation between the terminal voltage signal and the air gap signal. As the load angle increases, the phase voltage lag behind the rotor position (induced EMF) also increases.

That method gives stable results as can be seen in Fig. 3. It shows the change of load angle in the synchronous condenser, pumping and generating regimes, with varying active and reactive power.

EXISTING METHODS OF DETECTING THE GENERATOR LOSS OF SYNCHRONISM

Over 30 years ago, the electrical centers of power systems were located in the transmission networks whose protections detected the losses of synchronism without the need of shutting down generators. Over the years, transmission networks got stronger, but so did the generator and block-transformer impedances. This resulted in moving electrical centers of the system all the way to block-transformers and generators, thus connecting the strains of the mentioned system components.
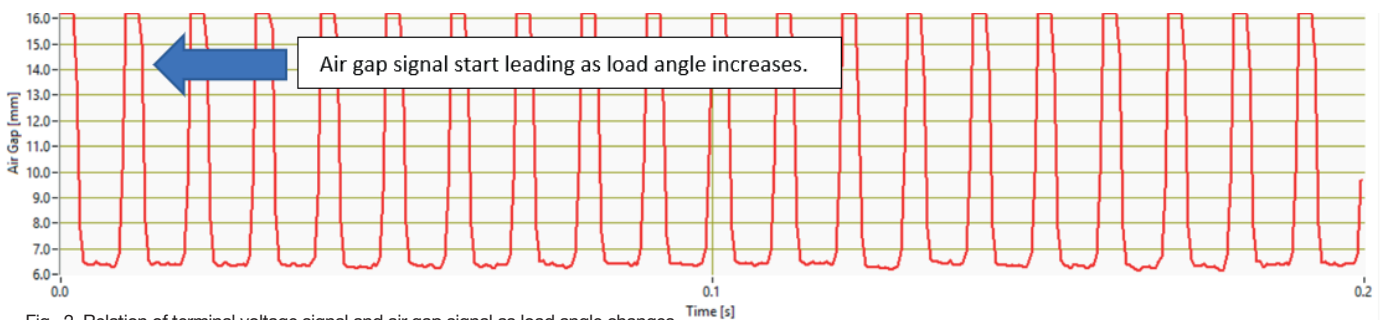

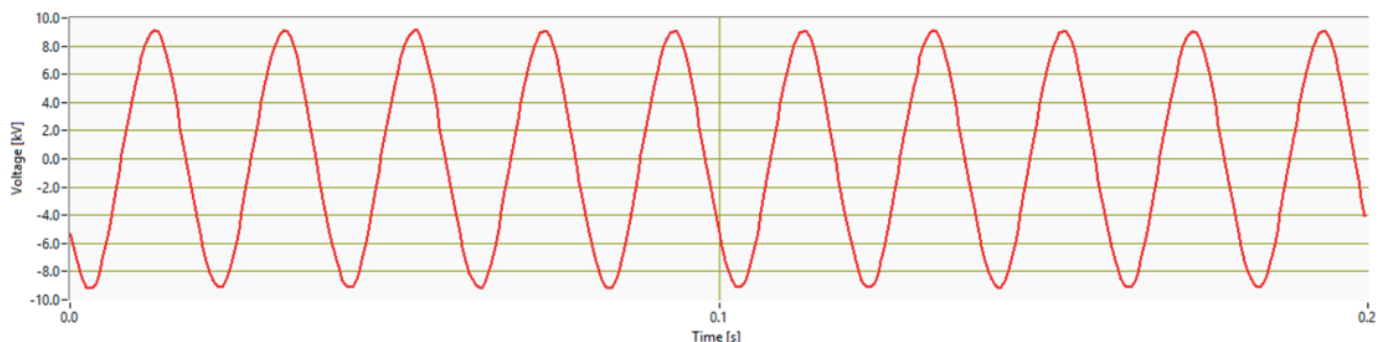Fig. 2. Relation of terminal voltage signal and air gap signal as load angle changes

Fig. 3. Change of load angle as active and reactive power change in time

In such a system, the loss of synchronism will not be detected by network protections, and the need for the loss of generator synchronism protection emerged. The existing generator protections, such as the differential protection or the overcurrent protection will not work in such situations. [2] The loss of excitation detection function can detect some loss of synchronism, but will not work in all situations in the system. The term "loss of synchronism" is closely tied to the term "transient generator stability". Transient stability deals with the issue of equalized processes through the phenomenon of attenuated oscillations of the angular rotor speed of synchronous machines, such as sudden load changes, changes of switching state and short circuits in the network. Transient stability is maintained if the oscillations are attenuated and the drive is returned to normal. In the case of transient stability, as well as static stability, there is a mutual dependence on the power transmitted and the generator load angle. In normal drive situations, this angle is constant and it depends on the load. In power swing situations, the angle oscillates, and when the loss of synchronism occurs, the angle can vary between 0 and 360 degrees [11],[12].

In the majority of modern numeric relays, the loss of synchronism function is realized through the measurement of impedance change in time. In the algorithms of this protection function, the passing of impedance vectors through the polygonal impedance characteristics is observed. The impedance is calculated from the positive sequence fundamental frequency components of the three voltages and currents. In Fig. 4. one typical out-of-step polygon is presented. It is described by impedances Za, Zb, Zc and Zd. The poygon is symmetrical about its vertical axis. The origin of coordinate system represents the point of measurement of currents and voltages. Zb is measured in reverse direction into the generator. In forward direction Zc is measured into unit transformer and Zd into power network. Depending of electrical centre of power swing, the impedance vector is moving through characteristic 1 or 2 [16]. When the condition for the loss of synchronism is fulfilled, that is, when the impedance vector passes through the polygonal characteristic, a counter is activated and the stimulus for the loss of synchronism protection is activated. After the set number of passes of the impedance vector through the polygonal characteristic is exhausted, the command to switch off the circuit breaker, excitation and turbine is activated [13],[14].

As set out above, the out-of-step protection functions are based on measuring the impedance and analyzing the history of the impedance phasor at a certain point, usually on the generator terminals. Additionally, the evaluation of the generator stability based on the criteria of monotony, continuity and uniformity impedance demands a certain time for detecting the loss of generator synchronism [15]. The next chapter will describe the concept of the out-of-step synchronism protection based on the direct load angle measurement.
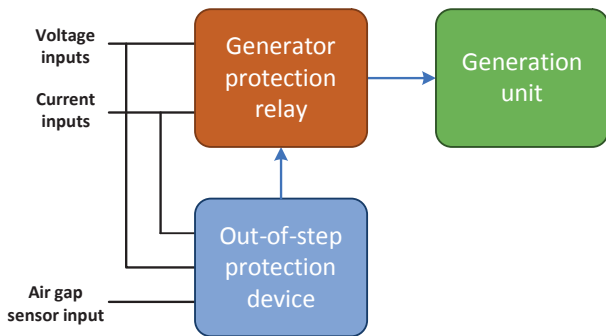

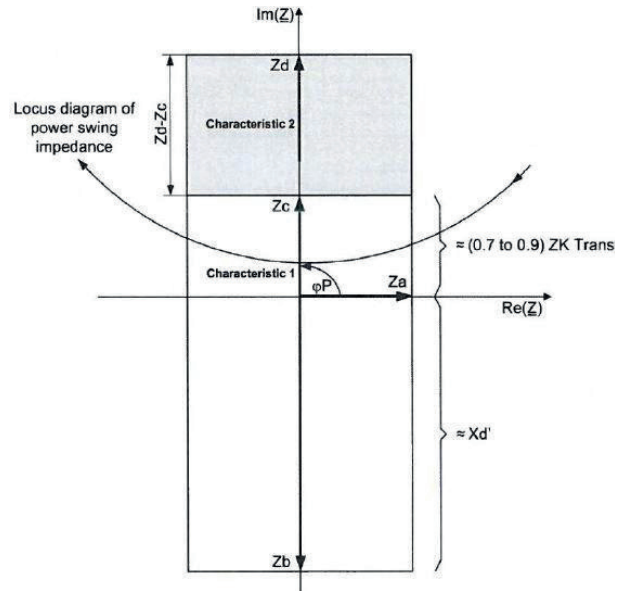Fig. 4. Example of a characteristic of out-of-step polygon

Fig. 5. Concept of the generator protection system with the separated out-of-step function

OUT OF STEP GENERATOR PROTECTION BASED ON THE DIRECT LOAD ANGLE MEASUREMENT

As previously mentioned, modern protections detect the loss of synchronism by measuring the impedance change, that is, by indirectly determining the generator load angle. On the other side, the load angle can be directly measured and such measurements are mostly used in the generator unit

monitoring systems [7]. In the monitoring systems, the load angle is calculated off-line on the basis of the collected measurements. For protection purposes, the load angle has to be calculated in real time and the calculations have to be performed with high accuracy and in short time intervals (every 20 ms). For easier understanding, the load angle calculation can be observed as the synchrophasor calculation. More details on the load angle measurements are given in Chapter 2. In our approach to the realization of the out-of-step generator protection function or the loss of synchronism by measuring the direct load angle, the air gap sensor method is used. The advantages of this method are also given in Chapter 2.

In the remainder of this chapter the approach or the idea behind the implementation of the out-of-step generator protection function by using the direct load angle measurement will be given. The main idea behind implementing this approach to the protection function is to develop a device that will encompass both the algorithm for measuring the load angle in real time and the algorithm for the out-of-step protection function. This device would be used alongside the usual generator protection relay and would detect the generator loss of synchronism faster than the standard relay protection function. Fig. 5. shows such a generator protection concept.

Unlike the calculation of the load angle for generator monitoring purposes, the measurement of the load angle in real time is much more complex for several reasons. To ensure the functionality of the protection algorithm, the load angle measurement has to be conducted every 20 to 40 ms.
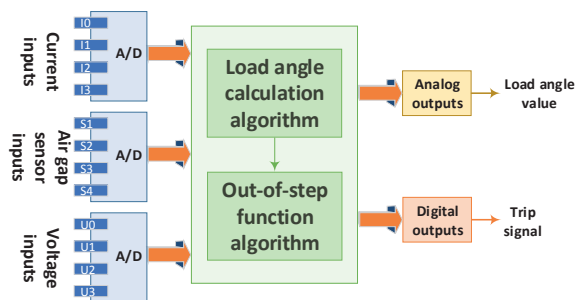

Fig. 6. The functional model of the development environment for testing the out-of-step protection function

Taking into account that the load angle is determined by measuring voltages and air gaps, it is very important to ensure the measurement precision, which on the other hand requires the processing of the measurement signal (voltage and air gap) to once again ensure the reliability and stability of the measurements. In applications where the processing time and calculation do not depend on the functionalities of the system (like monitoring) this does not represent a problem, but for generator protection purposes where only a short time interval is available for processing the signals and calculations and ensuring reliability, this is a challenge.

One of the main goals of this R&D project is to define the out-of-step generator protection function algorithm by measuring the direct load angle. In order to define and implement the protection algorithm in the development environment and to test it in the laboratory and in real conditions, a mathematical or simulation model for detecting the out-of-step generator protection has to be developed. The purpose of the simulation model is to enable the algorithm testing in certain operation states, and to determine, by using the simulation results, the algorithms' key parameters and its shortcomings. After defining the protection algorithm based on the conducted simulations and problem research, a functional model that will include all necessary functionalities of the device will be generated. The functional testing model for the out-of-step protection function is depicted in Fig. 6. The development environment is based on the National Instruments hardware and the LabVIEW simulation environment.

DIRECT LOAD ANGLE MEASUREMT METHOD

To ensure the functionality of the out-of-step protection algorithm, a very precise and reliable measurement of the load angle has to be provided. The rest of this chapter will present the testing results and describe the method developed for measuring the direct load angle of the synchronous generator.

The implementation of the load angle measurement algorithm functionalities includes the air gap measurement, generator voltage measurement, and rotor position detection. The main goal was to develop a method for measuring the load angle in real time which will provide a stable calculation or measurement of the load angle every 20 ms, or after each period. Because the load angle is a value determined in the same way as the phasor, that is the smallest possible resolution in which it can be measured or determined. When compared to the commonly used method for measuring the load angle shown in Chapter 2, this method takes into consideration the rotor imperfection. The rotor imperfection can be explained as a geometrical imperfection. This directly influences the precision of the air gap measurement, and consequently the load angle value. The geometrical imperfection of the rotor is in fact structural in nature, and is present in every generator. The imperfection is specific to every rotor and it is constant in
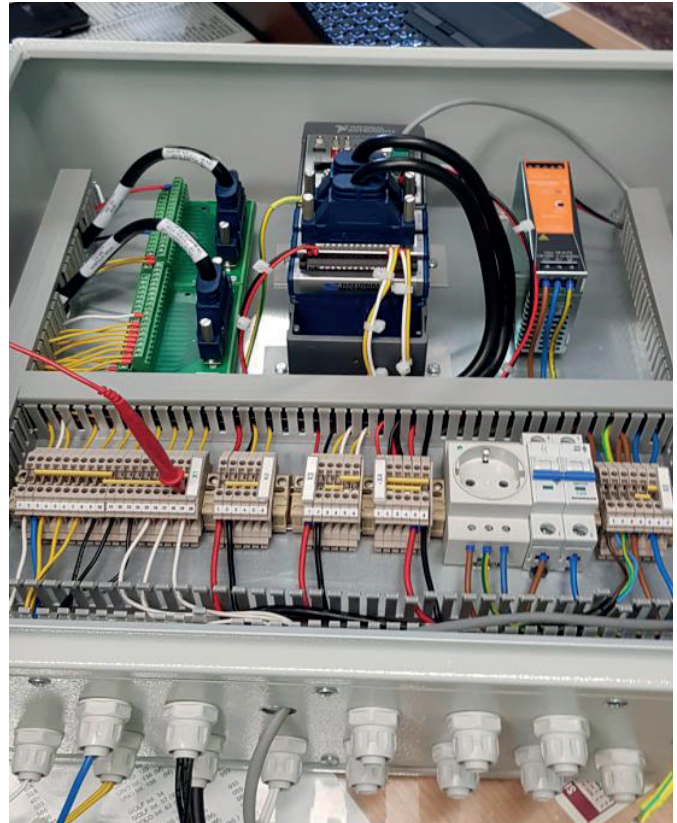
Fig. 9. Development environment for testing and direct load angle measurement

time, meaning it is possible to correct the air gap measurement for that specific imperfection. The characteristic of the deviation, which depends on the rotor position, has to be recorded in order to be applied in the direct load angle measurement algorithm. And to use this information in the algorithm, the rotor position first has to be determined. This is easily done by using the signal from the keyphasor sensor.

Fig. 7. shows the results of the direct load angle measurement without correcting the rotor geometrical imperfection, and Fig. 8. shows the re-

Fig. 7. Results of direct load angle measurement without geometrical imperfection correction

Fig. 8. Results of direct load angle measurement with geometrical imperfection correction

sults of the direct load angle measurement when the rotor geometrical imperfection is corrected. The results clearly show that correcting the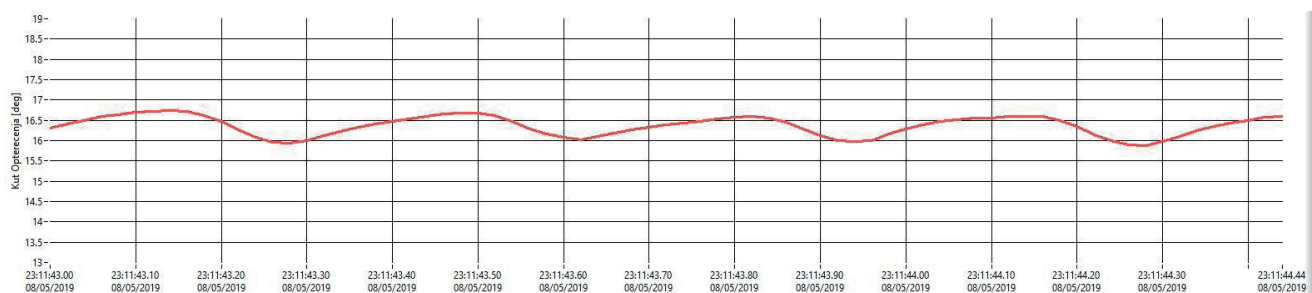 rotor geometrical imperfection improves the stability and accuracy of the direct load angle measurement of the synchronous generator.

The results presented here were obtained by measuring the direct load angle on a real hydro generator. The development environment where the functionalities for data gathering and processing from sensors, as well as the algorithm for determining the direct load angle, are shown in Fig. 9.

CONCLUSION

The development of the electricity market, new regulations and the development of the power network on the one hand, and high expectations on electricity supply and availability on the other hand make the power system increasingly more complex. Due to the mentioned factors, periods in which the operation of power system is on the upper edge of its capacity occur more frequently. To make sure the power system stays stable in such situations, advanced technologies that allow intelligent system management have to be used. Taking into account that the load angle is a very reliable indicator of stability, it should be considered for application in the power system protection.

This paper sets out a new approach to realizing the out-of-step generator protection function by measuring the direct load angle which is currently under development in the Pro Integris company. The project itself is in the initial phase so only a limited array of results and technical details were given. In this phase of the project, the algorithm for the real time load angle measurement and the mathematical generator model for testing the out-of-step protection algorithm by measuring the direct load angle are being developed. The real time load angle measurement algorithm testing results performed on a real hydro generator show a very precise and stable load angle calculation within the highest possible resolution. The development of the protection algorithm is a further goal of this project. After the conducted testing and the optimization of both algorithms, the project will set out to develop a functional model that will encompass both the real time load angle measurement algorithm and the out-of-step protection algorithm.

By applying the proposed approach to the out-of-step generator protection, the goal is to achieve faster detection of the loss of synchronism from the detection speed of the currently commercially available solutions. Although this solution demands an additional device next to the existing protection relay, and thus increased generator protection system costs, the benefits this investment incurs through faster detections of the loss of synchronism should justify the cost, considering the substantial malfunctions such a fault can cause.

ACKNOWLEDGMENT

REFERENCES

[1] S. Cheng, and M.S. Sachdev, "Out of Step Protection Using the Equal Area Criterion," Canadian Conference on Electrical and Computer Engineering, pp. 1488-1491, May 2005

[2] D. Reimert, "Protective relaying for power generation systems," Taylor & Francis, 2006

[3] J. Berdy, "Out of Step Protection for Generators," Electric Utilitiy Systems Engineering Department, General Electrc Company, New York

[4] M. Mišković, M. Mirošević, and G. Ergec, "Load Angle Estimation of a Synchronous Generator Usig Dynamical Neural Networks," Energija, vol. 58, No. 2, pp. 174-191, 2009

[5] M. Abedini, M. Davarpanah, M. Sanaye-Pasand, S.M. Hashemi, and R. Iravani, "Generator Out-of-Step Prediction Based on Faster-Than Real Tine Analysis: Concepts and Applications," IEEE Transactions on Power Systems, vol. 33, No. 4, 2018

[6] M. Jadrić, and B. Frančić, "Dinamika električnih strojeva," Graphis, Zagreb, August 1997

[7] M. Jadrić, B. Rajković, B. Terzić, M. Despalatović, Ž. Gladina, G. Orešković, B. Meško, and J. Macan, "Monitoring of Hydro Generator," FESB, Split, May 2004

[8] G. Orešković, and B. Meško, "HE Dubrava - Oscilacije snage i vlastite elektromehaničke frekvencije titranja agregata A i B," Veski and FER, Zagreb, 2004

[9] M. Despalatović, M. Jadrić, B. Terzić, and J. Macan, "On-Line Hydrogenerator Power Angle and Synchronous Reactances Determination Based on Air Gap Measurement," IEEE PES Power Systems Conference and Exposition, New York, vol. 2, pp. 753-758, 2004

[10] M. Jadrić, M. Despalatović, B. Terzić, and B. Rajković, "Metodologija za identifikaciju parametara sinkronog hidrogeneratora temeljena na mjerenjima u sustavu monitorniga," Automatika, vol. 48, pp. 9-19, Zagreb, 2007

[11] B. Filipović-Grčić, I. Ivanković, H. Bulat, and Z. Čerina, "Out of Step Generator Protection," 5. Savjetovanje HRO CIGRE, Cavtat, pp. 34-05, November 2001

[12] B. Filipović-Grčić, I. Ivanković, and R. Vlajčević, "Out of Step Protection in the Transmission Network," 6. Savjetovanje HRO CIGRE, Cavtat, pp. B5-06, November 2003

[13] D.A. Tziouvaras, and D. Hou, "Out of step protection fundamentals and advancements," SEL, 2003

[14] N. Kumar, D.R. Nagaraja, and H.P. Khincha, "A smart and adaptive scheme for generator out of step protection," IEEE Innovative Smart Grid Technologies - Asia (ISGT ASIA), Bangkok, pp. 1-6, 2015

[15] "SIPROTEC 5 Generator Protection 7UM85 Manual," Siemens AG, Nurnberg, 2018

[16] SIPROTEC 4 Generator Protection 7UM62 Manual," Siemens AG, Nurnberg, 2017

Denisa Galzina
Croatian Transmission System
Operator (HOPS PrP Zagreb)
Denisa.Galzina@hops.hr

Tonko Garma
FESB, University of Split
garma@fesb.hr

Flicker Spreading In a Transmission Networks

SUMMARY

This paper reports the flicker spreading in the transmission network. Chapter 1 presents introduction containing brief background and key concepts, followed by description of the corresponding instrumentation in Chapter 2. Key contribution of the paper is elaborated in Chapters 3 and 4. Chapter 3 reports measurements of the flicker magnitude along the 400 kV, 220 kV and 110 kV transmission grid for various distances from flicker origin on 400 kV grid, and Chapter 4 gives cost-effective predictive model, enabling estimation of the flicker magnitude for arbitrary selected origin-to-spot distance base on non-linear regression approach. Paper is extension of the work presented at Smagrimet 2019 conference.

KEYWORDS

Short term flicker (Pst), long term flicker (Plt), flicker origins, mitigation techniques, flicker mesurements, prediction model.

INTRODUCTION

According to EN50160 flickers are impressions of unsteadiness of visual sensation induced by a light stimulus, the luminance or spectral distribution of which fluctuates with time.

They are caused by rapid voltage changes, with amplitude much smaller than the sensitivity limit of electrical equipment. It could be said that most of the rapid voltage changes are actually flickers. The voltage flickering as low as 1% of the nominal voltage can already produce significant discomfort, especially if the frequency of the oscillation is between 8 and 10 Hz. [1] The voltage waveform during flicker occurrence measured at local wind power plant is given in Figure 1.
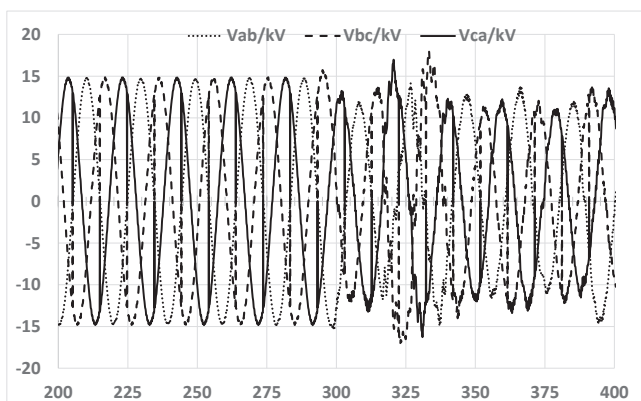

Figure 1. Voltage waveform during flicker occurence

The severity of flicker annoyance is defined by the UIE-IEC flicker measuring method and evaluated using two parameters [2]:

Parameter Pst, (short-term flicker) is measured for each 10-minute interval. Choosing the 10-minute observation period compromises the interval as long enough to prevent the emphasis on isolated cases of voltage variation and at the same time short enough to characterize the voltage changes caused by equipment with short working cycles.

Parameter Plt (long-term flicker) is calculated for a two-hour interval. Plt is derived from 12 consecutive Pst values according to equation:

$$P_{lt} = \sqrt[3]{\frac{\sum_{i=1}^{12} P_{st,i}^3}{12}}$$

(1)

Parameter Plt provides credibility for long-term flicker collection, when one must observe sources with long or variable work cycles, or when multiple sources of flicker work simultaneously in a random order.

Neither Pst nor Plt have a unit, but it corresponds to a limit that should not be passed in order not to cause discomfort the observer for any flicker.

Generally, it can be said that flickers are caused by devices with variable energy consumption, in particular reactive. Changes can occur by turning on or off large capacitive loads or for fluctuating loads, such as arc furnaces, industrial welding machines, or capacitor banks [3].

Various flicker models are reported in the existing literature. Most of them are focusing on the electric arc-furnaces as a dominant flicker occurrence source. In [4] the authors provide single phase arc-furnace model suitable for software-based time and frequency domain analysis. The aforementioned model is extended in [5], applying non-linear approach, based on both sinusoidal and with noise governed arc length variations. More recent study reported in [6] summarizes previous arc furnace models based on

both stochastic and chaotic approaches, and introduces the novel method based on voltage simulated by solving corresponding differential equations. This technique enables obtaining voltage-current characteristics and, furthermore, provides an arc current with harmonic spectrum consistent with the measured spectrum. Contrary to these models, eye and head model enable analysis of the flickers originating from various lamps, as reported in [7].

Since the existing literature, as reported in [4-7], focuses on flicker source modeling, or flicker behavior with respect to time [8], we believe this paper, reporting the flicker model enabling valuation and prediction of the flicker magnitude in terms of spot-to-origin distance, may be of interest to for the involved community.

This paper is organized in 5 Chapters. After introduction, flicker meter is briefly described, followed by the in-situ measurements. The crucial contribution of the paper is a model enabling prediction of the flicker magnitude bahvior with respect to corresponding origin distance. Finally, some conclusions are reported at the end of the paper.

FLICKERMETER

This chapter describes main characteristics and specification flicker meters should meet in terms of yielding usefull data. Standard IEC 61000-4-15 provides the functional and design specification for flicker measurement apparatus intended to indicate the correct flicker perception level for all practical voltage fluctuation waveforms. [9]

It is important to understand that the primary objective of the IEC flickermeter is not to provide an evaluation of voltage fluctuations but of flicker perception caused by these fluctuations. To achieve this goal, the equipment must be designed so that it can transform the input voltage fluctuations into an output parameter proportionally related to flicker perception. This is possible by simulating the process of physiological visual perception, that is the so-called lamp–eye–brain chain. [10] Figure 2 shows Block diagram of such flickermeter. [11]

EXAMPLE OF THE FLICKER SPREADING MEASUREMENTS THROUGH HIGH VOLTAGE GRID

There are few arc furnaces in the power network of the Croatian Transmission System Operator.

Since the ironworks is in an industrial environment, it is not possible to consistently track the spreading of voltage flickers through the grid. Therefore, we will observe the case of a 400 kV transmission line dropout, because of the relay protection activation. Measurements reported in this chapter are performed using commercially available PQ monitors equipped with the embedded flicker meter option, meeting the requirements reported in Chapter II. The monitors are obtained from well-known and reliable producers providing an extensive factory acceptance tests and warranties. In addition, monitors are regularly maintained in accordance to producer's manuals. In conclusion, set of power-quality measurements obtained using aforementioned devices is not limited in terms of research reported in this paper.

The transmission line was loaded with a current of about 300 A. At the time of the breakdown, the current increased to almost 3000 A (an increase of about 6 times the maximum power demand in that month, and about 10 times the current value immediately before the breakdown), as can be seen in Figure 3. Such an event generated a huge voltage flicker, exhibiting value of 2.7 measured on the 400 kV busbar, Figure 3.

Passing through the transformation of 400/220 kV, the flicker magnitude on the 220 kV side of the transformer decreased below 2 (Figure 4). Further transformation of 220/110 kV causes flicker magnitude to drop to about 1.8, as can be seen in Figure 5.
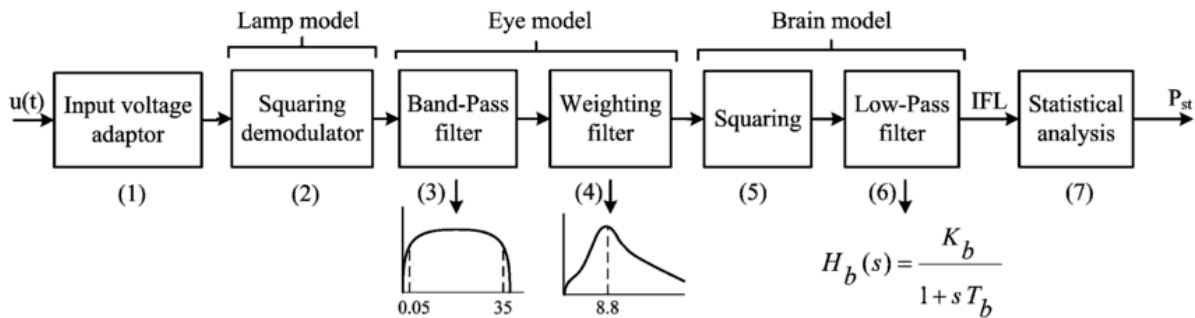

Figure 2.   Block diagam of a standard IEC flickermeter [11]

Block 1 of the flickermeter is an input voltage adaptor, which contains a voltage scaling circuit that accepts the supply voltage as an input and derives the relative voltage change.

Block 2 (lamp model part of flickermeter) is squaring demodulator, which recovers modulating signal from the sinusoidal carrier. Blocks 3 and 4 represent eye part of flickermeter. It is composed of a band pass filter and weighting filter. The brain model consist of blocks 5 and 6 – squaring and low pass filter. Squaring multiplier simulates human non-linear visual perception, and filter simulates the storage effect of the human brain. Block 7 conducts statistical analysis, using A/D convertor and classification of results. [11]
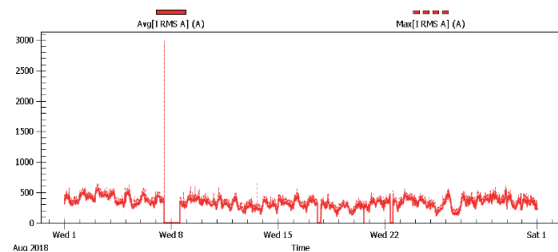

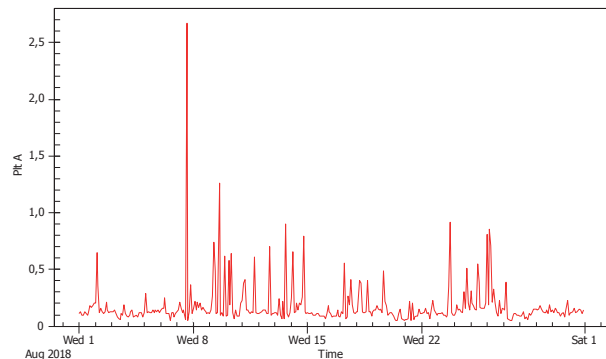Figure 3. Current values measured at 400 kV transmission line

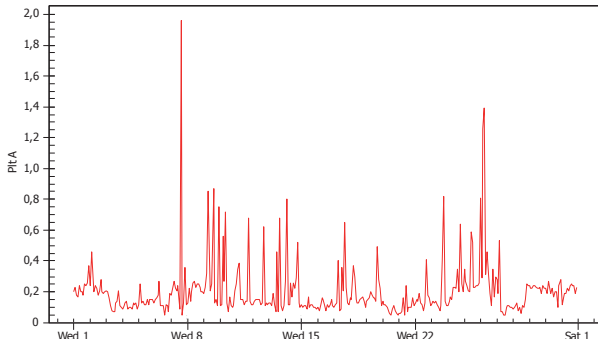Figure 4. Long term flicker at 400 kV transmission line during breakdown

Figure 5. Long term flicker at 220 kV lines after 400 kV lines breakdown

The flickers spread via transmission lines to the other 110 kV transformer stations. The closest station, TS B 110 / X kV, is positioned 9 km away from the source of disturbance, and the next, TS C 110 / X kV, is located 15 km further away, meaning, 24 km from the source. Transformer station D 110 / X kV is placed radially from the source of disturbance at a distance of 11 km.
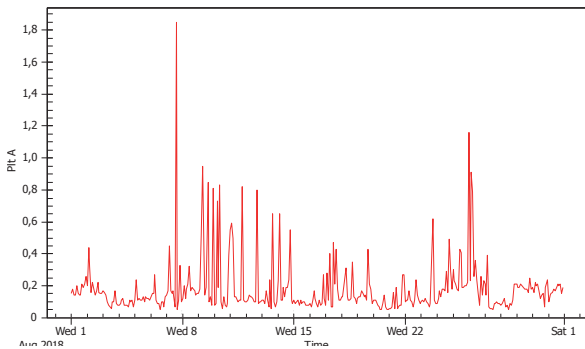

Figure 6. Long term flicker at 110 kV lines after 400 kV lines breakdow[n]

At the closest facility, TS B 110 / X kV, the flicker value is almost 1.6 (Fig 6). Upon arrival to the next (15 km distant) TS C 110 / X kV, the flicker value decreases to 1.5 (Figure 7).
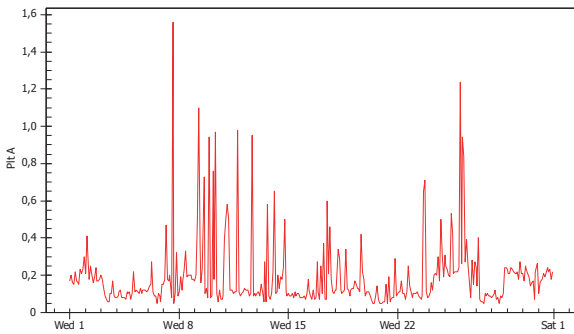

Figure 7. Long term flicker at 110 kV substation TS B, after 400 kV lines breakdown
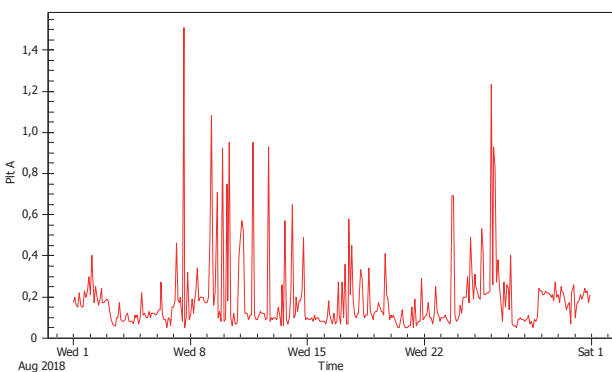

Figure 8. Long term flicker at 110 kV substation TS C, after 400 kV lines breakdown
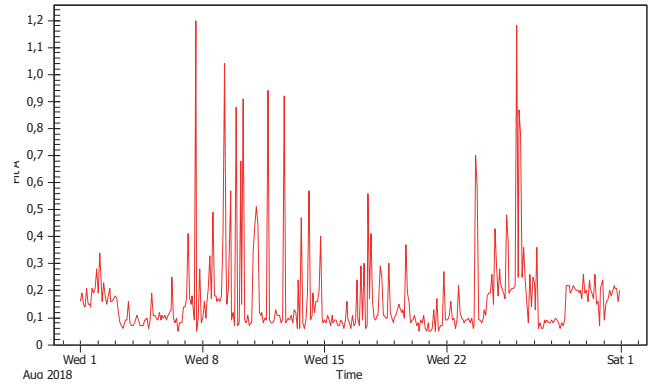

Figure 9. Long term flicker at 110 kV substation TS D, after 400 kV lines breakdown

In the radially located TS D 110 / X kV, 11 km away from the source of disturbance, the flicker value of 1.2 was measured. According to the graphs in Figures 3-8 it can be seen that at stations B and C (located at linearly separated positions) the flicker values decrease uniformly, while in the radially located station C the flicker value is less than what would be expected with respect to the distance from the source of the interference. That is because the substation C is, energetically, a much stronger substation, with transformers of much greater power.

Flicker values for all objects are given in Table 1.

Table I. Overview of Plt flicker according to the metering point

No	Substation	d[km]	S[MVA]	Plt
1	SS 400/220/110 kV	0	2 x 300	2,7 @ 400 kV
			1 x 400	2,0 @ 220 kV
				1,8 @ 110 kV
2	SS B 110/X kV	9	2 x 40	1,6
3	SS C 110/X kV	24	2 x 20	1,5
4	SS D 110/X kV	11	2 x 60	1,2

PREDICTIVE MODEL

In order to find the correlation between the flicker magnitude at an arbitrary selected location within analyzed transmission grid segment, regression analysis is applied. Analysis is executed upon measured flicker magnitudes obtained from PQ monitors permanently installed in 11 110/x kV substations located from flicker origin at distances up to 80 km.

Linear regression is based on the concept of linear curve describing the measured data. In general case regression curve is given by [12]:

$$\hat{y} = \beta_0 + \beta_1 x$$

(3)

The optimal line should be selected based on the minimum square criteria, while coefficients 0 and 1 are given by:

$$\beta_1 = \frac{\sum_{i=1}^{n} x_i y_i - n\overline{x}\overline{y}}{\sum_{i=1}^{n} x_i^2 - n\overline{x}^2}; \qquad \beta_0 = \overline{y} - \beta_1 \overline{x}$$

(4)

Nonlinear regression is characterized by the fact that the equation depends nonlinearly on one or more unknown parameters:

$$y_i = f(x_i, a_i) + \varepsilon_i, \; i = 1, 2, ..., n$$

(5)

where yi, f, xi, ai and εi stand for the response, the known function, the co-variant vector, the parameter vector, and the random errors, respectively. [12], [13] In our case f can be defined as exponential function:

$$f = a\ e^{-bd}$$

(6)

where f stands for the known function, a and b are coefficients while d represents the distance.

Based on the aforementioned approach, empirical model has been developed, enabling predictive analysis of the flicker magnitude for any given transmission system grid point placed between the flicker origin and the furthermost encompassed substation. Results of the model are reported in Figure 10. As it can be seen, the flicker magnitude decreases exponentially with respect to the distance from the origin.

Function describing the flicker behavior is obtained to be:

$$P_{lt} = 1,8999\ e^{-0,026\ d}$$

(7)

where d stands for distance in km and Plt is estimated long-term flicker magnitude. R2 parameter describing the quality of the model estimation exhibits value of 0,9943 out of 1,0000 proving acceptable accuracy and prediction power.
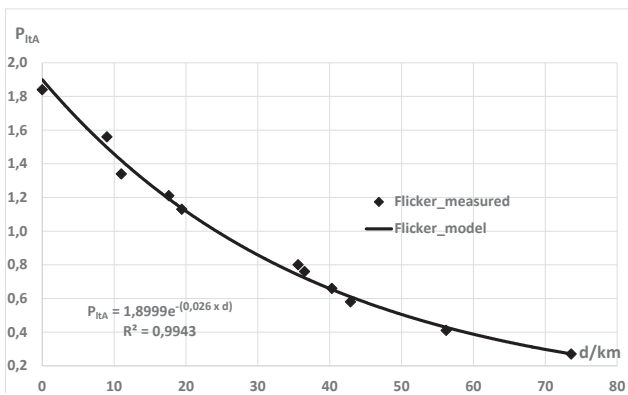

Figure 10. Graphical representation of the model enabling prediction of the flicker magnitude

For example, for a substation located 20 km from flicker origin, measured flicker magnitude is 1,13 while model yields prediction of 1,15 resulting in error of 1,5 %. Worst-case scenario error of less than 7 % obtained at 50 km from the source is attributed to fact that the corresponding substation(s) are linked via not only 110 kV, but also 400 kV lines. Table 2 reports comparison of the measurements and the model. Taking into account exponential decay of the flicker magnitude with respect to the distance from the origin, a linear decrease due to the linear increase of the line impedance could be expected. However, considering the well-known HV over-head power line behavior in transient conditions, observed exponential decay is not a surprise. [14]

Table 2. Comparison of the flicker magnitude obtained by measurements and the model

d[km]	Plt_measured	Plt_model	Error [%]
0,0	1,84	1,90	3,26
9,0	1,56	1,50	-3,62
11,0	1,34	1,43	6,52
17,6	1,21	1,20	-0,64
19,4	1,13	1,15	1,53
35,6	0,80	0,75	-5,89
36,5	0,76	0,74	-3,22
40,3	0,66	0,67	0,96
42,9	0,58	0,62	7,37
56,2	0,41	0,44	7,49
73,6	0,27	0,28	3,82

In addition to the model enabling the prediction of the flicker magnitude, flicker attenuation model is developed, providing the ability to estimate flicker attenuation rate with respect to arbitrary point-to-origin distance. We will define attenuation as follows:

$$A = 20 \log \left(\frac{m_i}{m_0} \right)$$

(8)

where A stands for attenuation in dB and mi and m0 are flicker magnitudes at arbitrarily selected point (within model scope) and origin, respectively. Assuming the attenuation defined as in eq. 8, the results reported in Figure 10 are obtained.
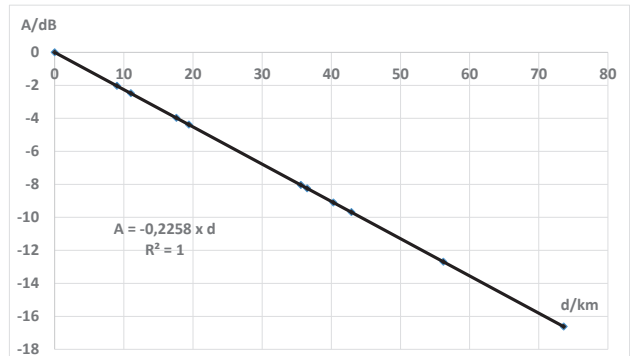

Figure 11. Graphical representation of the model enabling prediction of the flicker magnitude

As it can be seen on the graph, the flicker attenuation (in dB) with respect to the point-to-origin distance (in km), can be estimated as follows:

$$A = -0,2258 \times d$$

(9)

where d stands for distance in km and A is attenuation in dB. R2 parameter describing the quality of the model estimation exhibits value of 1.0 out of 1.0 proving supreme accuracy and prediction power. In other words, flicker attenuation rate is approximately 0,226 dB/km, meaning, flicker relative magnitude will decrease for value of 0,226 dB each km of its distance with respect to origin. According to the proposed model, for a previously mentioned SS located 20 km from the flicker origin, flicker magnitude will be slightly more than 60 % of its initial value.

CONCLUSION

Transmission system operator is obliged to maintain the parameters of voltage quality within the stipulated limits, in order to ensure that all the customers and network users receive the energy of a certain level. Even though flicker is technically not an issue of upmost relevance, customer's frequent complaints to the network operators, can have high financial consequences.

As expected, the measurement results reported in this paper, obtained from various substations within the grid, show clear decrease of the flicker magnitude with respect to source-to-point distance. Furthermore, measured data unambiguously exhibit severe flicker penetration deep into the grid, through multiple voltage levels (from 400 kV, over 220 kV, and then to 110 kV level), and causing the unadmitted levels of flicker in the substations up to 25 km away from the source of the flicker. In addition, aiming towards in-depth analysis of the flicker penetration radii, model based on non-linear regression has been developed, enabling the estimation of the flicker magnitude for any point of known source-to- point distance, contrasting the previously reported models based on flicker source modeling, or flicker behavior with respect to time. Proposed model is low-cost and low time-consuming tool enabling prediction of the flicker severity for analyzed grid segment with reasonable accuracy of 1-3 %. The worst-case scenario error of less than 7 %, obtained for origin-to-spot distance of around 50 km, is attributed to fact that the corresponding substation(s) are linked via not only 110 kV, but also 400 kV lines. Moreover, flicker attenuation model is reported, enabling estimation of the flicker magnitude drop with respect to initial value, and consecutive attenuation rate.

Considering the fact that radii of 25 km encompass up to 10 substations and that model for corresponding distance predicts flicker magnitude approximately 52 % of its initial value, transmission system operator can expect multiple customer's complaints. That forces the operators to maintain their facilities at high standard in order to supply the energy of sufficient voltage level quality.

ACKNOWLEDGMENT

REFERENCES

[1] UIE, "Connection of fluctuating load," Union Internationale d'Electrothermie / GDT Perturbations, 1988.

[2] C. G. Cornfield, "Definition and measurement of voltage flicker (in lighting)," in IEE Colloquium on Electronics in Power Systems Measurement, London, 1988.

[3] "Power quality in electrical systems, Power quality basics: Voltage fluctuation and flicker," [Online]. Available: http://www.powerqualityworld.com/2011/09/voltage-fluctuations-flicker.html.

[4] G. Manchur and C. Erven, "Development of a model for predicting flicker from electric arc furnances," IEEE Transaction on Power Delivery, 1992.

[5] G. Montanari, M. Loggini, A. Cavallini, L. Pitti and D. Zaninelli, "Arc-furnance model for the study of flicker compensation in electrical networks," IEEE Transaction on Power Delivery, 1994.

[6] O. Ozgun and A. Abur, "Flicker study using a novel arc furnance model," IEEE Transaction on Power Delivery, 2002.

[7] A. Emanuel and L. Peretto, "A simple lamp-eye-brain model for flicker observations," IEEE Transaction on Power Delivery, 2004.

[8] A. Girgis, J. Stephens and M. E:B:, "Measurement and prediction of the voltage flicker magnitude and frequency," IEEE Transaction on Power Delivery, 1995.

[9] IEC 61000-4-15 (1997-11), »Electromagnetic compatibility (EMC) – Part 4: Testing and measurement techniques – Section 15: Flickermeter – Functional and design specifications,« IEC, 1997.

[10] A. Baggini, Handbook of Power Quality, Wiley & Sons, 2008.

[11] P. Moallem, A. Zargari and A. Kiyoumarsi, " A practical framework for applying effects of various lamps on IEC flickermeter and evaluating results in a welding system," Journal-Chinese Institute of Engineers, pp. 421-429, 2012.

[12] G. Smyth, Nonlinear Regression, Encyclopedia of Environmetrics, Chichester: John Wiley & Sons, 2002.

[13] J. Chappell, S. P. Drake, C. L. Seidel, L. J. Gunn, A. Iqbal, A. Allison and D. Abbott, "Geometric Algebra for Electrical and Electronic Engineers," in IEEE Power Engineering Society Summer Meeting, Edmonton, 1999.

[14] F. Gatta, A. Geri, S. Lauria and M. Maccioni, "Backflashover simulation of HV transmission lines with enhanced counterpoise groundings," Electric Power Systems Research, 2009.

ENERGIJA